version 5/3/2021

Published as:

Cui H, Kitajima K, Orland IJ, Xiao S, Baele JM, Kaufman AJ, Denny A, Zhou C, Spicuzza MJ, Fournelle JH, Valley JW (2021) Deposition or diagenesis? Probing the Ediacaran Shuram Excursion by SIMS. Global and Planetary Change. 206: 103591, 36p. https://dx.doi.org/10.1016/j.gloplacha.2021.103591.

Ediacaran Shuram excursion modulated by methane oxidation: Insights from the Doushantuo Formation in South China

Huan Cui[1,2,3,4,*], Kouki Kitajima[4], Ian J. Orland[4,5], Shuhai Xiao[6], Alan J. Kaufman[7], Jean-Marc Baele[8], Adam Denny[4,9], Michael J. Spicuzza[4], John H. Fournelle[4], John W. Valley[3,4]

1. Equipe Géomicrobiologie, Institut de Physique du Globe de Paris (IPGP), Université de Paris, 75005 Paris, France
2. Stable Isotope Laboratory and CIFAR Earth 4D Group, Department of Earth Sciences, University of Toronto, Toronto, ON M5S 3B1, Canada
3. NASA Astrobiology Institute, University of Wisconsin, Madison, WI 53706, USA
4. Department of Geoscience, University of Wisconsin, Madison, WI 53706, USA
5. Wisconsin Geological and Natural History Survey, Madison, WI 53705, USA
6. Department of Geosciences, Virginia Tech, Blacksburg, VA 24061, USA
7. Department of Geology and Earth System Science Interdisciplinary Center, University of Maryland, College Park, MD 20742, USA
8. Department of Geology, Faculty of Engineering, University of Mons, 7000 Mons, Belgium
9. Pacific Northwest National Laboratory, Richland, WA 99354, USA

*Corresponding author: Huan.Cui@ipgp.fr (H. Cui); Current address: IPGP, Université de Paris, Paris, France. https://orcid.org/0000-0003-0705-3423

Abstract

The largest carbon isotope ($\delta^{13}C$) negative anomaly preserved in bedded carbonates — the Ediacaran Shuram Excursion (SE) — shows values down to ca. –10‰ on a global scale. Notably, $\delta^{13}C$ profiles of the SE in South China are highly variable among correlative sections, which challenges the conventional view of a homogeneous dissolved inorganic carbon (DIC) reservoir. It has been suggested that authigenic carbonates with distinct $\delta^{13}C$ values may have caused the chemostratigraphic variability. However, studies that focus on authigenic carbonates in the SE of South China on a micrometer scale are still limited. Here, following a recent SIMS study on the Doushantuo Formation at the intra shelf Jiulongwan section, we expand our scope to the outer shelf environment (Zhongling and Yangjiaping sections). Two samples from the upper Zhongling section are newly investigated by cathodoluminescence (CL), micro X-ray fluorescence (μXRF), scanning electron microscope (SEM), and secondary ion mass spectrometry (SIMS) in this study. The new results reveal remarkable spatial heterogeneity in $\delta^{13}C$ on a micrometer scale with extremely negative values down to –37.5‰ (VPDB). We propose that the heterogeneous SE in South China is manifest at both micrometer and basinal scales, and was modulated by methane oxidation in variable local redox conditions. In the intra shelf environment, seawater DIC of the restricted basin was mixed with methane-derived alkalinity in anoxic/euxinic water column, leading to the formation of typical SE in bedded carbonates (e.g., the Jiulongwan section). In the more oxygenated outer shelf environment, methane-derived authigenic calcite formed within shallow marine sediments via microbial sulfate reduction (MSR) and anaerobic oxidation of methane (AOM), causing the preservation of strong isotopic contrast in carbonates of different generations (i.e., the Zhongling and Yangjiaping sections). Our study demonstrates that integrated SEM–SIMS analysis is an effective approach to assessing the origin and diagenetic history of $\delta^{13}C$ anomalies in sedimentary record.

1. INTRODUCTION

The Neoproterozoic Era witnessed profound fluctuations in carbonate carbon isotope ($\delta^{13}C_{carb}$) compositions (Kaufman et al., 1997; Halverson et al., 2005). Notably, the Ediacaran Shuram Excursion (SE) — named after the Shuram Formation in Oman — shows $\delta^{13}C_{carb}$ values down to ca. –10‰ (VPDB) on a global scale (Burns and Matter, 1993; Fike et al., 2006; Grotzinger et al., 2011). Similar and perhaps time-equivalent excursions have also been reported from the upper Doushantuo Formation in South China (Jiang et al., 2007; McFadden et al., 2008; Wang et al., 2012; Zhou et al., 2012; Lu et al., 2013; Zhu et al., 2013; Zhou et al., 2017).

Notably, published studies of the SE in South China reveal variable chemostratigraphic $\delta^{13}C_{carb}$ profiles among correlative sections (Zhu et al., 2007b; Lu et al., 2013; Zhu et al., 2013; Cui et al., 2015; Wang et al., 2016; Li et al., 2017; Zhou et al., 2017; Wang et al., 2020). The SE is most typical in the Yangtze Gorges area (e.g., Jiulongwan section, Xiangdangping section) and is commonly referred to as EN3 (Zhou and Xiao, 2007; McFadden et al., 2008) or DOUNCE (Zhu et al., 2007a; Lu et al., 2013; Zhu et al., 2013). In contrast, consistent chemostratigraphic expression of Shuram-like $\delta^{13}C_{carb}$ values of –9‰ is lacking at the outer shelf sections (Macouin et al., 2004; Ader et al., 2009; Kunimitsu et al., 2011; Cui et al., 2015; Furuyama et al., 2016; Cui et al., 2017) and upper slope sections (Wang et al., 2016; Li et al., 2017). Given that the residence time (~100 kyr) of dissolved inorganic carbon (DIC) is much longer than the seawater mixing time (Wallmann and Aloisi, 2012), shallow marine $\delta^{13}C_{DIC}$ should be homogeneous across contemporaneous platforms. Therefore, the strong heterogeneity in SE-equivalent sections in South China challenges the conventional view that the SE carbonates record a homogeneous marine DIC reservoir.

One hypothesis that aims to explain the above enigma proposes that authigenic (i.e., formed in situ) carbonate that is precipitated along sediment-water interface during early diagenesis may have played a significant role in causing variable $\delta^{13}C_{carb}$ excursions in deep time (Schrag et al., 2013). Based on this hypothesis, various proportions of isotopically distinct authigenic carbonate that formed within shallow marine sediments could lead to strong heterogeneity in bulk $\delta^{13}C_{carb}$ values. Indeed, methane-derived authigenic calcite nodules with strong ^{13}C depletion along with admixed fine-grained calcite and dolomite have been reported from South China and are linked to the SE (Cui et al., 2017). However, most of the published studies on Neoproterozoic $\delta^{13}C_{carb}$ excursions in South China are based on either bulk or micro-drilled powders (e.g., Kaufman and Knoll, 1995; Halverson et al., 2005; Jiang et al., 2007; McFadden et al., 2008), which essentially reflect homogenized signals of multiple stages of carbonate precipitation. Studies that focus on carbonates at a micrometer scale are still limited.

In recent years, in situ analysis of sedimentary carbonates by secondary ion mass spectrometer (SIMS) has emerged to be a powerful tool in unravelling the detailed diagenetic histories and their corresponding $\delta^{13}C_{carb}$ signals of deep-time carbonate record (Śliwiński et al., 2016b; Andrieu et al., 2017; Denny et al., 2017; Śliwiński et al., 2017; Cui et al., 2019; Xiao et al., 2019; Denny et al., 2020; Husson et al., 2020; Xiao et al., 2020). Following our recent SIMS investigation of the SE in the uppermost Doushantuo Formation at the intra shelf Jiulongwan section (Cui et al., 2021), here we expand our view towards the outer shelf environment by revisiting the upper Doushantuo Formation at Zhongling and Yangjiaping (Fig. 1). Two samples from the upper Zhongling section were newly analyzed in this study by using integrated techniques, including optical microscope, micro X-ray fluorescence (μXRF), cathodoluminescence (CL), scanning electron microscope (SEM), and secondary ion mass spectrometer (SIMS). The main goals of this study are (1) to further investigate the SE at outer shelf region in an unprecedented spatial resolution of a μm scale; (2) to compare the SIMS $\delta^{13}C_{carb}$ results of the intra shelf Jiulongwan section and the outer shelf Zhongling section; and finally, (3) to propose a unifying biogeochemical model for the variable SE in South China.

2. BACKGROUND

2.1. Geological background

The Ediacaran Doushantuo Formation in the Yangtze block of South China overlies the Nantuo diamictite and begins with a ca. 635 Ma Marinoan cap carbonate (Fig. 1) (Condon et al., 2005; Jiang et al., 2011). Stratigraphically above the Doushantuo Formation is the dolostone-dominated Dengying Formation. The age of the Doushantuo–Dengying boundary was originally constrained to be ca. 551 Ma (Condon et al., 2005), but was later revised to be slightly older based on a more recent stratigraphic re-correlation (An et al., 2015; see also Zhou et al., 2017 for a different view).

Deposition of the Doushantuo Formation can largely be divided into two stages, beginning with an open ramp shelf that gradually transitioned into a rimmed shelf protecting an intra shelf lagoon (Jiang et al., 2011; Cui et al., 2015). Stratigraphic data and paleogeographic reconstructions indicate an increase in water depth from proximal intertidal environments in the northwest to distal deep basinal settings in the southeast. Three platform facies belts have been proposed, including a proximal inner shelf dominated by peritidal carbonates, an intra shelf lagoon containing mixed carbonates and shales, and an outer shelf shoal complex consisting of carbonates and phosphorites (Fig. 1) (Jiang et al., 2011).

In the field, the upper 50 meters of the Doushantuo Formation at Zhongling and Yangjiaping is mainly composed of intraclastic, oolitic, or fine-grained carbonate facies associated with discrete levels of

phosphorite, suggesting deposition in an outer shelf carbonate shoal environment (Jiang et al., 2011; Cui et al., 2015; Cui et al., 2016; Cui et al., 2017). Based on the occurrence of phosphatic allochems and oolite, the bedded fine-grained dolostone and phosphorite likely formed in well agitated seawater, and then dolomitized in the outer-shelf environment during very early diagenesis (Cui et al., 2016; Cui et al., 2017).

The Doushantuo dolostones are often pervasively fine grained, which indicates a primary or early diagenetic origin. Indeed, earlier studies suggest that the composition of Precambrian ocean may be very different from the Phanerozoic ones and can facilitate the precipitation of primary dolomite (Tucker, 1982; Hood and Wallace, 2012; Hood et al., 2015; Hood and Wallace, 2018). Notably, largely based on a clumped isotope study, dolostones of the Doushantuo Formation at the inner shelf Zhangcunping section have been interpreted to result from syndepositional (i.e., early diagenetic) dolomitization near sediment-water interface (Chang et al., 2020).

A striking feature of the upper Doushantuo Formation at Zhongling and Yangjiaping is the occurrence of ^{13}C-depleted authigenic calcite nodules and cements (Macouin et al., 2004; Ader et al., 2009; Kunimitsu et al., 2011; Cui et al., 2016; Furuyama et al., 2016; Cui et al., 2017). These authigenic calcite have been interpreted as an early diagenetic origin and formed in shallow marine sediments (Macouin et al., 2004; Ader et al., 2009; Macouin et al., 2012; Cui et al., 2016; Furuyama et al., 2016; Cui et al., 2017). Extremely negative $\delta^{13}C_{carb}$ values down to ca. –37‰ (VPDB) were found in these nodules (Fig. 2E, 2I), suggesting a significant contribution from the oxidation of biogenic methane (Cui et al., 2017).

Late calcite veins have also been found in the Zhongling section, but they typically crosscut the primary sedimentary beddings and show moderate $\delta^{13}C_{carb}$ values (from ca. –5 to ca. +6‰) (Cui et al., 2017). Therefore, we rule out any causal link — both isotopically and petrographically — between these late calcite veins and the ^{13}C-depleted authigenic calcite (Cui et al., 2017). In addition, no mineralogical evidence for metamorphic alteration or massive recrystallization has been observed in the field or thin sections. Therefore, we preclude the possibility that the outer shelf sections have been significantly affected by late hydrothermal activities.

2.2. Chemostratigraphy based on micro-drilled or bulk powders

Detailed chemostratigraphy of the intra shelf section (Jiang et al., 2007; McFadden et al., 2008; Li et al., 2010; Sawaki et al., 2010; Zhou et al., 2012; Ling et al., 2013; Tahata et al., 2013; Shi et al., 2018) and the outer shelf sections (Macouin et al., 2004; Zhu et al., 2007b; Ader et al., 2009; Li et al., 2010; Kunimitsu et al., 2011; Furuyama et al., 2016; Cui et al., 2017) have been published based on conventional

analyses of micro-drilled or crushed bulk powders (e.g., Fig. 2). The sampling holes induced by micro-drilling is typically 800 μm in diameter (Cui et al., 2015; Cui et al., 2017). Before the introduction of more detailed SIMS study, an overview of the published chemostratigraphic results of the Doushantuo Formation is necessary. Here, we briefly summarize the main chemostratigraphic features below.

$\delta^{13}C_{carb}$ chemostratigraphy. — The $\delta^{13}C_{carb}$ profile of the Doushantuo outcrops at Jiulongwan shows three notable Ediacaran Negative (EN) excursions: EN1 in the basal cap carbonate, EN2 in the middle section, and EN3 at the top (Jiang et al., 2007; McFadden et al., 2008; Li et al., 2010). More recent studies based on drill cores or outcrops reveal more nuanced excursions (Tahata et al., 2013; Zhu et al., 2013), complicating the stratigraphic correlation within the basin. Notably, EN2 has been proposed to be correlative with the middle Ediacaran Gaskiers glaciation (Kunimitsu et al., 2011; Tahata et al., 2013; Furuyama et al., 2016), although this age assignment still remains ambiguous (Narbonne et al., 2012; Xiao et al., 2016).

The EN3 interval in the Yangtze Gorges area typically shows a sudden decrease of $\delta^{13}C_{carb}$ from +5‰ down to ca. –9‰ (VPDB) within ca. 20 meters, and then the $\delta^{13}C_{carb}$ values remain as low as ca. –9‰ stratigraphically upward for around 40 meters before recovering back to positive values (Fig. 2A) (Jiang et al., 2007; Zhou et al., 2012; Ling et al., 2013; Lu et al., 2013; Tahata et al., 2013). This profound $\delta^{13}C_{carb}$ negative excursion has been correlated with the SE on a global scale (Jiang et al., 2007; McFadden et al., 2008).

The $\delta^{13}C_{carb}$ profiles of the carbonate matrix in the upper Doushantuo Formation at Zhongling and Yangjiaping show scattered and only a few moderately negative data points (ranging from +7 to –7‰) in the upper 60 meters (Fig. 2E, 2I). However, it is notable that white-colored authigenic calcite nodules and cements in the upper part of these two sections preserve remarkably negative $\delta^{13}C_{carb}$ values down to ca. –37‰ (Fig. 2E, 2I) (Macouin et al., 2004; Zhu et al., 2007b; Ader et al., 2009; Macouin et al., 2012; Cui et al., 2016; Furuyama et al., 2016; Cui et al., 2017). Viewed together, the carbonate matrix and the authigenic calcite show a much wider range of $\delta^{13}C$ in the upper Doushantuo Formation at these two outer shelf sections (Fig. 2E, 2I).

$\delta^{18}O_{carb}$ chemostratigraphy. — The $\delta^{18}O_{carb}$ profile of the EN3 interval at Jiulongwan shows an overall negative excursion down to –10‰ (Fig. 2B), which broadly co-varies with the $\delta^{13}C_{carb}$ profile (Fig. 2A). The $\delta^{18}O_{carb}$ profiles at Zhongling and Yangjiaping show small variations between ca. –2 to ca. –9‰, with authigenic calcites that tend to be more negative (ca. –9‰) in $\delta^{18}O$ than the carbonate matrix (Fig. 2F, 2J).

$\delta^{34}S$ chemostratigraphy. — Sulfur isotope data measured from the Jiulongwan EN3 interval show a progressive decrease from ca. +30 to ca. +10‰ in carbonate-associated sulfate ($\delta^{34}S_{CAS}$) (Fig. 2C) (McFadden et al., 2008; Li et al., 2010; Shi et al., 2018). In the meanwhile, pyrite S isotope ($\delta^{34}S_{pyrite}$) data in the EN3 interval at Jiulongwan show a parallel decrease from ca. 0 to –20‰ (Fig. 2C) (McFadden et al., 2008; Li et al., 2010; Shi et al., 2018). The coupled decreases from paired S isotopes suggest higher sulfate concentrations and sulfide availability during EN3 (McFadden et al., 2008; Li et al., 2010; Shi et al., 2018). Notably, a stratified ocean with a dynamic euxinic wedge maintained on an open shelf has been proposed for the Jiulongwan section (Li et al., 2010), but this model was later revised to be a restricted euxinic water mass developed in an intra shelf lagoonal environment (Cui et al., 2015).

The $\delta^{34}S$ profiles of the upper Doushantuo Formation at Zhongling and Yangjiaping show exclusively positive values of around +20‰ (Fig. 2G) (Li et al., 2010; Cui et al., 2015; Cui et al., 2017). The $\delta^{34}S_{CAS}$ data in the upper Zhongling section show consistent values ca. +40‰ (Li et al., 2010). Compared with the Jiulongwan section, the paired $\delta^{34}S_{pyrite}$ and $\delta^{34}S_{CAS}$ data at Zhongling and Yangjiaping mimic the data of pre-EN3 intervals at Jiulongwan. This has been interpreted as either a sulfate gradient in the ocean (Li et al., 2010; Li et al., 2017) or a potential stratigraphic truncation or non-deposition near the top of the Doushantuo Formation in the outer shelf region (Cui et al., 2015).

$^{87}Sr/^{86}Sr$ chemostratigraphy. — The $^{87}Sr/^{86}Sr$ profile of the Jiulongwan section shows a notable rise from ca. 0.7080 to 0.7090 in the EN3 interval (Fig. 2D), suggesting enhanced chemical weathering during the SE. Similar increases in $^{87}Sr/^{86}Sr$ have also been reported from other SE-equivalent strata on a global scale (Burns et al., 1994; Calver, 2000; Le Guerroué et al., 2006; Melezhik et al., 2009; Cui et al., 2015). The $^{87}Sr/^{86}Sr$ profile of the upper Doushantuo Formation at Zhongling was mainly measured from methane-derived authigenic calcite nodules and cements, which shows a slight increase from 0.7080 to 0.7083 in the upper 50 meters (Fig. 2H) (Cui et al., 2017). $^{87}Sr/^{86}Sr$ profile of the upper Yangjiaping section show a similar increase from 0.7080 to 0.7085 (Fig. 2L). Compared with the Jiulongwan section, the lack of more radiogenic $^{87}Sr/^{86}Sr$ values of ca. 0.7090 at the Zhongling and Yangjiaping sections has been interpreted to result from a potential stratigraphic incompleteness in the shallow shelf rim environment (Cui et al., 2015).

2.3. Redox constraints

Fe speciation results of the Doushantuo Formation at Jiulongwan suggest that the EN3 interval was deposited in an overall anoxic intra shelf environment with intermitted euxinic episodes and increasing sulfide availability (see Fig. S6 in Li et al., 2010). This inferred anoxic/euxinic redox conditions for the EN3 interval at Jiulongwan is also consistent with the published cerium anomaly (Ce/Ce*) data, which show a

progressive increase from ca. 0.3 to ca. 0.8 across EN3 and also suggest more reducing redox conditions (Zhou et al., 2012; Wei et al., 2018).

On a global scale, U isotope ($\delta^{238}U$) results of the SE suggest an extensive oceanic oxygenation event. Profiles of the SE at the Jiulongwan section of South China, the Bol'shoy Patom section of Siberia, the Death Valley succession of the southwestern United States, and the Sonora Succession in northwestern Mexico, all reveal significant positive shifts from ca. −0.73‰ to ca. −0.27‰, which has been interpreted as a major oceanic oxygenation event (Zhang et al., 2019; Li et al., 2020). It should be noted that this inferred global oceanic oxygenation event during the SE does not necessarily conflict with the local anoxia/euxinia in intra shelf environment based on the Fe speciation and Ce/Ce* data of the Jiulongwan section. As emphasized by Li et al. (2020), "there is no irreconcilable contradiction between local anoxia and extensively enhanced ocean oxygenation, as shown by the modern ocean in which anoxic basins exist locally despite generally oxic conditions globally". Therefore, although the $\delta^{238}U$ data suggest an extensive oceanic oxygenation event in the global open ocean, the local redox proxies (including Fe speciation, Ce anomaly) of the Doushantuo Formation at Jiulongwan suggest an overall anoxic/euxinic redox conditions during EN3.

Compared with the extensively studied Jiulongwan section, geochemical data that can directly infer redox conditions of the Zhongling section are limited. Nevertheless, sedimentological results of the Zhongling and nearby Yangjiaping sections show abundant carbonate intraclasts, oolite, and phosphorite intraclasts in the upper part of the Doushantuo Formation (Jiang et al., 2011; Kunimitsu et al., 2011; Cui et al., 2017), suggesting an overall shallow, dynamic, and probably well oxygenated depositional environment during carbonate or phosphorite deposition. In contrast, no intraclast, oolite, or any cross bedding has been found in the upper Doushantuo Formation at Jiulongwan (Jiang et al., 2007; McFadden et al., 2008). Therefore, sedimentological results of the upper Zhongling section suggest an overall shallower and more oxygenated environment during deposition than the upper Jiulongwan section.

3. SAMPLES AND ANALYTICAL METHODS

3.1. SIMS samples

Following the recent SIMS study of the upper Doushantuo Formation at the intra shelf Jiulongwan section (Cui et al., 2021), here we focus on the outer shelf Zhongling section in order to obtain a basin-wide view on the SE in South China (Fig. 1). Two SIMS epoxy mounts from a dolostone sample at Zhongling were newly analyzed by integrated μXRF, SEM, CL, and SIMS (Fig. 3; Table 1). In situ $\delta^{13}C$ analysis of both calcite and dolomite was conducted on a CAMECA IMS 1280 at the Wisconsin Secondary Ion Mass

Spectrometer (WiscSIMS) Laboratory, University of Wisconsin–Madison, USA. The spot-to-spot reproducibility of $\delta^{13}C_{carb}$ values based on all bracketing analyses of the calcite standard UWC3 is ±1.1‰ (2SD; 7-μm beam size). Detailed geochemical data are available in the online supplemental materials.

3.2. Micro X-Ray Fluorescence

High-resolution elemental abundance maps of the polished sample surfaces were produced using the M4 Tornado micro X-ray Fluorescence (μXRF) scanner (Bruker nano GmbH, Berlin, Germany) at the Vrije Universiteit Brussel, Belgium. μXRF mapping was performed along a 2D grid with 25 μm spacing, a spot size of 25 μm and an integration time of 1 ms per pixel. The X-Ray source was operated under maximum energy settings (600 μA, 50 kV) with no source filters. This mapping approach by μXRF resulted in qualitative element concentration distributions on the elemental maps.

3.3. Cathodoluminescence

Cathodoluminescence excitation was achieved with a cold-cathode CITL CL system (Cambridge Image Technology – model Mk5, UK) in the Department of Geology, University of Mons, Belgium. The instrument was operated at 15 kV acceleration voltage, 500 μA beam current, and a current density of about 8 $\mu A/mm^2$. CL images were captured with a Peltier-cooled digital color camera (Lumenera model Infinity 3, Canada) set from 0.1 s to a few seconds exposure time depending on the CL intensity and microscope magnification. Multiple-frame averaging was used to reduce noise. Color calibration of the camera (white balance) was performed using the blue-filtered, tungsten-halogen light source of the microscope, which may result in CL colors that are slightly different from other equipment (especially around the yellow band, which is narrow), but ensures more or less standardized observation conditions.

3.4. SIMS carbonate carbon isotope analysis

In situ $\delta^{13}C_{carb}$ analysis of both calcite and dolomite was conducted on a CAMECA IMS 1280 at the Wisconsin Secondary Ion Mass Spectrometer (WiscSIMS) Laboratory, Department of Geoscience, University of Wisconsin–Madison. During SIMS analysis, carbon stable isotopes (^{12}C, ^{13}C) were measured with a 7-μm-diameter beam size. These analyses were made using one Faraday cup and two electron multiplier detectors measuring $^{12}C^-$, $^{13}C^-$, and $^{13}C^1H^-$, respectively. The WiscSIMS reference material UWC3 calcite was used as a running standard (Fig. 9) (Kozdon et al., 2009; Valley and Kita, 2009; Śliwiński et al., 2016a). Measured ratios of $^{13}C/^{12}C$ were calculated as "raw" δ-values ($\delta^{13}C_{raw}$) before converting to the VPDB scale typically based on eight analyses of UWC3 that bracket each group of 10–15 sample analyses. Carbon isotope ratios are reported in standard per mil (‰) notation relative to VPDB, calculated as $\delta^{13}C_{sample} = [(^{13}C/^{12}C)_{sample} / (^{13}C/^{12}C)_{VPDB} - 1] \times 1000$. The spot-to-spot reproducibility of $\delta^{13}C_{carb}$ values,

calculated from all bracketing analyses on UWC3, is ±1.1‰ (2SD, 7 μm spots). All raw and corrected SIMS data are reported in the online supplementary materials.

Measurements of $^{13}C/^{12}C$ were made using a $^{133}Cs^{+}$ primary ion beam with an intensity of ~600 pA. The secondary ion intensity of ^{12}C was ~7×10^{6} cps and was used as a monitor of quality control during analysis. SIMS spots with aberrant count rates were not included in the figures or considered in data interpretation but are listed in the online appendix. ^{13}CH was analyzed simultaneously with ^{13}C and ^{12}C also as a quality control to evaluate the effect of hydrogen on SIMS analysis, which might be related to the presence of organic matter or water as discussed in previous carbonate SIMS studies (Denny et al., 2017; Wycech et al., 2018). An electron flood gun in combination with a gold coating (~40 nm) was used for charge compensation. The total analytical time per spot was about 4 minutes including pre-sputtering (20 s), automatic centering of the secondary ion beam in the field aperture (60 s), and analysis (160 s). The baseline noise level of the Faraday cups was monitored during pre-sputtering.

After SIMS analysis, Fe concentration (Fe# = molar ratio of Fe/[Fe+Mg]) adjacent to each SIMS pit was measured by EPMA to correct the composition-specific instrumental mass fractionation (IMF or bias) of each SIMS $\delta^{13}C_{carb}$ analysis. Typically, for the correction of each raw SIMS $\delta^{13}C_{carb}$ value, an averaged Fe# value was calculated based on the elemental concentration data of two or three EPMA spots that are close to the corresponding SIMS pit. Although constraining the underlying controls on IMF is challenging, it has been found that raw $\delta^{13}C_{carb}$ data obtained by SIMS could be biased by IMFs that vary in magnitude depending on instrumental conditions, mineralogy, and sample composition (Valley and Kita, 2009; Śliwiński et al., 2016a). To address the effect of Fe/Mg on IMF, a suite of standards along the dolomite–ankerite series were analyzed at the beginning of each session and used to generate a calibration curve relative to the dolomite standard UW6220 (Fig. 10) (Śliwiński et al., 2016a). The calibration curve was used to determine the composition-specific IMF and to correct $\delta^{13}C$ value for each SIMS pit (see online appendix Excel File: SIMS data spreadsheet). As discussed in detail by Śliwiński et al. (2016a), the empirical calibration of IMF for Ca–Mg–Fe carbonates varies with session-specific instrument tuning and running conditions. Therefore, as applied elsewhere (Denny et al., 2020), different IMF vs. Fe# curves were calibrated in each session to correct $\delta^{13}C_{carb}$ data (Fig. 10). EPMA data show that the Zhongling calcite is very low in Fe, Mn, and Mg concentration, with average values of $FeCO_3$ mol% = 0.00, $MnCO_3$ mol% = 0.00, $MgCO_3$ mol % = 1.08 (n=52, Table 3). Therefore, the SIMS $\delta^{13}C$ data analyzed from Zhongling calcite were corrected for IMF using data from UWC3. All raw and corrected SIMS data, EPMA data, and quality control methods are reported in the online supplementary materials.

3.5. Scanning electron microscope

After SIMS analysis, the gold coating was removed and replaced with an iridium coat for Scanning Electron Microscope (SEM) imaging in the Ray and Mary Wilcox SEM Laboratory, Department of Geoscience, University of Wisconsin–Madison. BSE images of samples were acquired with a Hitachi S3400 VP SEM with EDS using a Thermo Fisher thin window detector. Each pit was investigated by SEM for possible irregularities. SEM images were acquired using an accelerating voltage of 15 keV or 20 keV at a working distance of 10 mm. All the SIMS pits were imaged by SEM and are shown with corresponding $\delta^{13}C_{carb}$ values in the online supplementary materials.

3.6. Electron probe microanalysis

EPMA was performed on the CAMECA SX–51 at the Cameron Electron Microprobe Laboratory at the University of Wisconsin–Madison. Data were collected with a ~120 second analysis time and a 15 keV, 20 nA beam, which was defocused to a 5 μm diameter in an attempt to minimize sample damage. Data were processed using EPMA software (Donovan et al., 2018), and background correction was performed with the Mean Atomic Number procedure (Donovan and Tingle, 1996). As changes over time in measured intensities are common for EPMA measurements in carbonates, particularly for the element Ca, a self-fitted time-dependent intensity correction was applied for all elements (Donovan et al., 2018). CO_2 was added for the matrix correction, based upon the appropriate C:O ratio, with oxygen determined by stoichiometry to the cations. The matrix correction used was PAP, with Henke mass absorption coefficients. Standards used were Delight Dolomite (Mg), Callender Calcite (Ca), siderite (Fe), rhodochrosite (Mn) and strontianite (Sr). Samples and standards were coated with ~200 Å carbon. WDS X–ray intensities were acquired with EPMA software, with mean atomic number backgrounds and with the PAP matrix correction, iterated within the matrix correction.

4. RESULTS

4.1. Petrographic and micro-drilled results

SEM observation reveals distinct textures of calcite and dolomite at Jiulongwan and Zhongling. The SE-equivalent EN3 interval at Jiulongwan largely consists of dolomitic limestone with calcite microspar (ca. 5–10 μm in size) as the matrix and zoned dolomite crystals (<10% volumetrically based on petrographic observations) (Cui et al., 2021). Thin dolostone layers have also been found in the lower EN3 interval, and they consist mostly of euhedral to subhedral dolomite crystals under SEM (Cui et al., 2021).

Micro-XRF and optical petrographic results in this study (Figs. 3–5; Table 2) show that the Zhongling dolostone consists of alternating laminations between dolomite-dominated lamina (with dolomite up to 99.8%) and authigenic-calcite-rich lamina (with calcite up to 39.1%). Integrated with the previously published micro-drilled data (Cui et al., 2017), it is revealed that the authigenic-calcite-rich lamina typically shows more negative $\delta^{13}C$ values in micro-drilled powders (Fig. 3A; Table 2). Notably, a pure calcite nodule in the bottom of the slab shows $\delta^{13}C$ value of –34.1‰ (VPDB) (Fig. 3A). It seems that the mixing of authigenic calcite in dolomite during micro-drilling can lower the overall $\delta^{13}C$ values of the micro-drilled powders in conventional isotope analysis by gas-source isotope ratio mass spectrometer (GS–IRMS). However, a direct test of this speculation requires in situ analysis by SIMS (see the next section).

SEM results show that the Zhongling dolostone consists of uniformly fine-grained (ca. 30 μm in size), homogeneous, anhedral dolomite crystals with non-planar boundaries (Figs. 8A–C, 13–15). Under CL, the Zhongling dolomite shows distinct green and red luminescence in different generations (Figs. 5; 13–15; online supplementary materials). Green luminesce from dolomite has been rarely reported in published literature. Nevertheless, it has been proposed that the green color in dolomite may reflect early dolomitization with a fast precipitation rate in an evaporative environment (Gillhaus et al., 2010), which is consistent with an outer shelf environment for the Zhongling section.

In contrast, the authigenic calcite at Zhongling appears as clean (i.e., inclusion-free), sparry cements precipitated within the dolomite matrix (Figs. 4, 5, 8, 13–15) and typically shows dull luminescence under CL (Fig. 5, 13–15). A trace amount of authigenic quartz cements have also been found in the authigenic-calcite-rich laminae (Figs. 3D–E, 8D–I). These authigenic quartz crystals typically form together with authigenic calcite, and have euhedral shape and distinct crystal terminations (Figs. 8D–I).

4.2. SIMS $\delta^{13}C$ results

SIMS calcite standard UWC3 was repeatedly analyzed between every 10 to 15 unknown samples in order to monitor running conditions. The $\delta^{13}C$ values of UWC3 in the course of SIMS analysis show highly consistent values (Fig. 9), suggesting steady running conditions. Cross plots of SIMS $\delta^{13}C$ values vs. Fe, Mn, and Mg concentration data show no clear correlation (Fig. 11), suggesting little influence of instrumental mass fractionation (IMF) on the SIMS $\delta^{13}C$ data. Compared with the recently analyzed SIMS and EPMA data of the Jiulongwan EN3 samples (Cui et al., 2021), the Zhongling samples show very low concentration of Fe (Fe# = 0.00 in all the dolomite data; Appendices 4, 5); therefore, the IMF caused by Fe on the SIMS $\delta^{13}C_{dolomite}$ data should be minimum. Indeed, only 0.5‰ of bias (from –58.5 to –59‰ in Fig. 11C, 11F) was found in the Zhongling $\delta^{13}C_{dolomite}$ data.

SIMS $\delta^{13}C$ results of the SE calcite and dolomite from intra shelf Jiulongwan and outer shelf Zhongling show distinct ranges of values (Figs. 12, 16). The Jiulongwan SIMS $\delta^{13}C$ data show values from –9.5 to –6.2‰ (mean –8.2‰, n=36, 2SD=1.51‰) in calcite microspar and values from –11.2 to –3.8‰ (mean –7.8‰, n=91, 2SD=2.93) in dolomite (Cui et al., 2021). In striking contrast, the Zhongling SIMS $\delta^{13}C$ data show a much wider range (from –37.5‰ in calcite to +4‰ in dolomite, n=79). The Zhongling dolomite crystals show mostly positive values (mean +2.0‰, n=25, 2SD=2.29‰), whereas the Zhongling authigenic calcite cements show extremely negative values down to –37.1‰ (mean –23.2‰, n=54, 2SD=16.08‰) (Table 5).

It is notable that the new SIMS data reveal remarkable spatial heterogeneity of $\delta^{13}C$ in authigenic calcite cement on a micrometer scale (SIMS data 2SD=16.08‰, n=54). In some cases, the $\delta^{13}C$ values vary up to ca. 20‰ over ~20 μm (from –36.0 to –16.6‰ in calcite, Fig. 13A; from –37.1 to –18.3‰ in calcite, Fig. 13A), or up to ca. 39‰ over ~30 μm (from –36.0‰ in calcite to +2.7‰ in dolomite, Fig. 13A).

5. DISCUSSIONS

5.1. Origin of authigenic calcite

The most striking feature of the Doushantuo Formation at Zhongling and Yangjiaping is the occurrence of white-colored, ^{13}C-depleted authigenic calcite nodules and cements (Fig. 2E, 2I) (Macouin et al., 2004; Zhu et al., 2007b; Ader et al., 2009; Macouin et al., 2012; Cui et al., 2016; Furuyama et al., 2016; Cui et al., 2017). Interpreting the origin of these authigenic calcite requires a careful evaluation of its paragenesis. Here we discuss this issue based on our earlier study (Cui et al., 2017) and the new results in this study. Multiple lines of field, petrographic, and geochemical evidence suggest that the authigenic calcite is early diagenetic (pre-compaction) in origin and formed via microbial sulfate reduction (MSR) and anaerobic oxidation of methane (AOM) through cement precipitation and/or replacement of preexisting dolomicrite.

First, authigenic calcite at the upper Doushantuo Formation at Zhongling are all preserved as sparry cement or nodules within fine-grained dolostones and intraclastic phosphorites (Cui et al., 2017). These authigenic calcite cements and nodules are exclusively aligned with sedimentary bedding in the field, and they are mostly isolated from each other and are not associated with any late crosscutting calcite veins. It is notable that all the authigenic calcite nodules show a thin rim of authigenic quartz, which has been interpreted as resulting from a pH variation in porewater during early diagenesis (Cui et al., 2017). We regard that the a trace amount of authigenic quartz cements (Fig. 8D–I) in the calcite-rich laminae may bear the same origin.

Second, no evidence for hydrothermal fluids was found to be closely associated with authigenic calcite. We indeed noticed some late calcite veins that vertically crosscut sedimentary bedding in the field, but those veins show mildly negative $\delta^{13}C_{calcite}$ values (ca. –5‰) (Cui et al., 2017), and are therefore unlikely to be the source of the ^{13}C-depleted authigenic calcite.

Third, the Zhongling authigenic calcite shows $^{87}Sr/^{86}Sr$ values of ca. 0.7081 to 0.7083 (Cui et al., 2017), which are comparable to Ediacaran seawater signals based on the consistency of $^{87}Sr/^{86}Sr$ compositions within the SE from a global compilation (see Fig. 17 in Cui et al., 2020). The dolomite matrix normally shows slightly higher $^{87}Sr/^{86}Sr$ values, which may be due to the loss of Sr during dolomitization, and the addition of ^{87}Sr from ^{87}Rb decay in admixed clay minerals.

Fourth, the new SIMS data reveal remarkable spatial heterogeneity of $\delta^{13}C$ in authigenic calcite on a micrometer scale (Figs. 13–15). In some cases, the $\delta^{13}C_{carb}$ values vary up to ca. 20‰ over ~20 μm (from –36.0 to –16.6‰ in calcite, Fig. 13A; from –37.1 to –18.3‰ in calcite, Fig. 13A), or up to ca. 39‰ over ~30 μm (from –36.0‰ in calcite to +2.7‰ in dolomite, Fig. 13A). The spatial heterogeneity of $\delta^{13}C$ on a micrometer scale is unlikely to represent intruded hydrothermal fluid signals but may result from the progressive generation of cement modulated by local microbial activity and the variable mixture of seawater and methane-derived alkalinity.

Fifth, elemental analyses of the authigenic calcite nodule samples show much higher Sr concentration and much lower Fe, Mn, and Rb concentration than their dolomite matrix (Cui et al., 2017). The authigenic calcite nodules are rich in Sr (mean value: 1681 ppm; n=6), whereas the Mn/Sr and Rb/Sr ratios of measured authigenic calcite nodules are all near zero (Cui et al., 2017). These elemental results support an early diagenetic origin for the authigenic calcite.

Sixth, both the Zhongling and Yangjiaping sections show very similar sedimentological textures and geochemical signals (Fig. 2E, 2I). These two sections are around 4 km in distance. Although it is possible that a potential hydrothermal event can influence both sections, the fact that these methane-derived authigenic calcites were exclusively found in the same interval (i.e., the uppermost Doushantuo and the basal Dengying formations; see the next section for detailed discussion) at both sections indicates that authigenic calcite mineralization was a depositional event.

Based on the above evidence, an early diagenetic origin with active sulfate-driven AOM occurring in pore fluids of shallow marine sediments is preferred for the ^{13}C-depleted calcite in the upper Doushantuo Formation at outer shelf regions.

5.2. Stratigraphic correlation

A basin-wide comparison of the SE in the uppermost Doushantuo Formation reveals variable chemostratigraphic profiles among different sections in South China (Zhu et al., 2007b; Lu et al., 2013; Zhu et al., 2013; Cui et al., 2015; Wang et al., 2016; Li et al., 2017; Zhou et al., 2017; Wang et al., 2020). The SE at the Jiulongwan section (i.e., EN3) show consistent Shuram-like values of –9‰ in stratigraphy (Fig. 2A). In contrast, such a feature is lacking at the outer shelf Zhongling and Yangjiaping sections (Fig. 2E, 2I). Instead, highly negative $\delta^{13}C$ values have been found in the upper Doushantuo and basal Dengying formations (Fig. 2E, 2I). This basin-scale heterogeneity of $\delta^{13}C_{carb}$ profiles in the uppermost Doushantuo Formation has been attributed to various reasons, including a stratigraphic truncation or non-deposition in outer shelf regions (Cui et al., 2015), various availability of oxidant for microbial sulfate reduction (MSR) (Li et al., 2017), local facies variation, diagenesis, and/or a cryptic unconformity (Zhou et al., 2017).

The stratigraphic correlation between the EN3 interval at Jiulongwan (Fig. 2A) and the much more expanded $\delta^{13}C_{carb}$ excursions at the upper Zhongling (Fig. 2E) and Yangjiaping sections (Fig. 2I) is not straightforward. Given the lack of direct geochronological constraints from these sections, their stratigraphic correlation largely relies on $\delta^{13}C_{carb}$ and $^{86}Sr/^{86}Sr$ chemostratigraphy. Two schemes of stratigraphic correlation between these two sections have been proposed, including one that correlates the upper 50 meters of the Zhongling section with the EN3 interval at Jiulongwan, and a more conservative view that correlates only the upper 15 meters of the Zhongling section to the EN3 interval (see Fig. S7 in Li et al., 2010).

The potential existence of stratigraphic truncation, non-deposition, or faulting around the upper Doushantuo Formation may further complicate the correlation across the basin. It is notable that, although the Doushantuo Formation at Zhongling (260 m) is much thicker than that at Jiulongwan (160 m), an integrated chemostratigraphic study suggests that the top of the Doushantuo Formation in outer shelf region may have been stratigraphically truncated or with no deposition on the top (Cui et al., 2015). More recently, it was proposed that the variable stratigraphic expression of $\delta^{13}C_{carb}$ excursions in upper Doushantuo could be caused by multiple factors, including local facies variation, diagenesis, and/or potential unconformities (Zhou et al., 2017).

Despite the above-mentioned factors that may inhibit a direct correlation for the $\delta^{13}C_{carb}$ excursions in the upper Doushantuo Formation, we regard that the timing of the $\delta^{13}C_{carb}$ negative excursions at Zhongling and Yangjiaping, including those extremely ^{13}C-depleted methane signals (Fig. 2E, 2I), should not be substantially different from that of the Jiulongwan EN3 interval. Although the middle and lower Zhongling section was also thoroughly investigated in the field, no calcite nodules (and thus extremely low

452 $\delta^{13}C_{carb}$ signals) were found. It appears that the massive mineralization of early diagenetic methane-derived
453 authigenic calcite was a pulsed event that only occurred during the deposition of the upper Doushantuo and
454 the basal Dengying formations.

455 It needs to be noted that the division of the Doushantuo and Dengying formations at Yangjiaping
456 is not always consistent in the published literature. Some studies used the discrete phosphorite interval as
457 the marker bed for the uppermost Doushantuo Formation (Zhu et al., 2007b; Jiang et al., 2011; Cui et al.,
458 2015; Cui et al., 2017); whereas some other studies placed the Doushantuo–Dengying boundary slightly
459 higher based on the termination of the $\delta^{13}C_{carb}$ negative excursion (Macouin et al., 2004; Ader et al., 2009;
460 Kunimitsu et al., 2011; Furuyama et al., 2016). If we accept the former scheme, then negative $^{13}C_{carb}$ signals
461 also appear in the basal Dengying Formation (Fig. 2I); if we accept the later, all the negative $^{13}C_{carb}$ signals
462 are limited to the Doushantuo Formation. The Zhongling section bears very similar features. Authigenic
463 calcite at Zhongling has also been found in the fine-grained, gray dolostone interval immediately above the
464 uppermost phosphorite layer of the Doushantuo Formation (Cui et al., 2017), although they have not been
465 analyzed for $\delta^{13}C_{carb}$ values. It needs to be emphasized that the Doushantuo–Dengying boundary is likely
466 to be diachronous across the basin, and the above different schemes of stratigraphic division do not affect
467 our interpretation.

468 In summary, although multiple factors could complicate the direct correlation between the intra
469 shelf and outer shelf sections, we propose that the overall negative $\delta^{13}C_{carb}$ excursion at Zhongling and
470 Yangjiaping (including those highly ^{13}C-depleted methane signals measured from authigenic calcite) are
471 broadly correlative to the SE at Jiulongwan. Therefore, there may be a causal link between these $\delta^{13}C_{carb}$
472 anomalies, which we will explore further in the next section.

473 **5.3. Biogeochemical model**

474 Viewed in detailed petrographic and stratigraphic context, we propose that the SIMS $\delta^{13}C$ data at
475 Zhongling and Jiulongwan reflect a wide spectrum of sedimentary processes (Fig. 17). In the shallow outer
476 shelf environment, the mostly positive $\delta^{13}C_{dolomite}$ values at Zhongling (ranging between +0.2 and +4.0‰,
477 with a single outlier at –1.5‰) likely represent open marine DIC signals, while the much more negative
478 $\delta^{13}C_{calcite}$ values (–37.5 to –9.3‰) likely result from microbial sulfate reduction (MSR) and anaerobic
479 oxidation of methane (AOM) in shallow marine sediments. Due to the restricted nature of pore space in
480 shallow marine sediments, those highly ^{13}C-depleted methane-derived alkalinity could not be fully mixed
481 with seawater, and therefore were preserved in situ as authigenic calcite cements or nodules (Fig. 17C).

In the intra shelf environment (i.e., Jiulongwan section), the much narrower range of $\delta^{13}C_{carb}$ values (mean ca. –9‰) in the EN3 interval likely result from a mixing of seawater DIC (i.e., +5‰) with methane-derived alkalinity (i.e., ca. –40‰) within a restricted basin (Fig. 17B). In this view, methane flux from the deeper methanogenesis zone in the sediment escapes to the seafloor, being oxidized by seawater sulfate, and consequently decreases the $\delta^{13}C_{DIC}$ of the intra shelf basin. Based on a simple two-endmember mixing calculation (Fig. 18), mixing seawater DIC ($\delta^{13}C_{DIC}$ = +5‰) with ca. 35% of methane-derived alkalinity ($\delta^{13}C_{methane}$ = –40‰) can generate Shuram-like values of ca. –10‰.

Based on the above interpretations, the $\delta^{13}C_{carb}$ variability at Jiulongwan and Zhongling was, therefore, potentially caused by two different sedimentary processes (Fig. 17). The Jiulongwan EN3 interval results from the mixing of seawater DIC with methane-derived alkalinity above the seafloor of a restricted basin (Fig. 17B), whereas the much larger variation in $\delta^{13}C_{carb}$ at Zhongling reflects the mineralization of methane-derived alkalinity within porewater of shallow marine sediments (Fig. 17C), which is resolved by SIMS for the first time in this study.

Here, we propose that variable local redox conditions may have also played a role in causing these heterogeneous $\delta^{13}C$ excursions. Previous studies suggest that the Jiulongwan section was deposited in an overall anoxic intra shelf environment with intermitted euxinic episodes (Li et al., 2010), while the Zhongling section was deposited in a shallower and oxygenated outer-shelf environment (Cui et al., 2015) (Fig. 17A). In this scenario, anoxia/euxinia with continuous supply of sulfate flux from the continent may have facilitated MSR and AOM in water column (Fig. 17B). In contrast, the more oxidizing redox condition at Zhongling may have driven MSR, AOM, and the sulfate-methane transition zone (SMTZ) below the sediment-water interface (Fig. 17C).

In light of this study, the heterogeneous chemostratigraphic profiles of the SE in South China were likely caused by the confluence of various environmental factors. In euxinic basins where methane oxidation occurs in the water column, this $\delta^{13}C$ excursion is manifest as the typical SE (ca. –9‰) and relatively muted variations at micrometer scale (Fig. 12A). In contrast, in more oxic environments where methane oxidation occurs in sediments, this excursion exhibits much greater spatial heterogeneity at micrometer scale (Fig. 12B, 13–15). These findings challenge the view that the SE records global ocean $\delta^{13}C_{DIC}$ values. Instead, the globally recorded SE may represents local expressions of a widespread event that was modulated by methane oxidation in anoxic/euxinic basins along continental margins.

6. CONCLUSIONS

Following a recent SIMS study on the Doushantuo Formation at the intra shelf Jiulongwan section (Cui et al., 2021), we expanded our scope to the outer shelf environment (Zhongling and Yangjiaping sections). Two samples from the upper Zhongling section were newly investigated by cathodoluminescence (CL), micro X-ray fluorescence (μXRF), scanning electron microscope (SEM), and secondary ion mass spectrometry (SIMS) in this study.

In strong contrast with the Jiulongwan SIMS data that show a relatively narrower range (from –11.2 to –3.8‰, n=127) (Cui et al., 2021), the new SIMS results of Zhongling samples reveal a wide range of $\delta^{13}C$ values (from –37.5‰ in calcite to +4.0‰ in dolomite, n=79), with remarkable spatial heterogeneity in $\delta^{13}C$ on a micrometer scale. Extremely negative values down to –37.5‰ have been analyzed from authigenic calcite cements, suggesting the contribution of biogenic methane.

We propose that the heterogeneous SE in South China is manifest at both micrometer and basinal scales, and resulted from the modulation of methane oxidation in variable local redox conditions. In the intra shelf environment, seawater DIC in the restricted basin was mixed with methane-derived alkalinity in anoxic/euxinic water column, leading to the formation of typical SE in bedded carbonates (e.g., the Jiulongwan section). In the more oxygenated outer shelf environment, methane-derived authigenic calcite formed within shallow marine sediments via microbial sulfate reduction (MSR) and anaerobic oxidation of methane (AOM), causing strong isotopic contrast in carbonates of different generations (i.e., the Zhongling and Yangjiaping sections). Our study demonstrates that integrated SEM–SIMS analysis is an effective approach to assess the origin and diagenetic history of $\delta^{13}C$ anomalies in sedimentary record.

ACKNOWLEDGEMENTS

The authors thank Bil Schneider for assistance in the SEM laboratory; Brian Hess, Noriko Kita, James Kern, and Maciej Śliwiński for assistance in sample preparation and SIMS analysis; Huifang Xu for assistance in the microscopic laboratory; Niels J. de Winter and Steven Goderis for guidance in the μXRF laboratory; Yiheng Wu for assistance in compiling supplemental materials; Chuanming Zhou for field assistance and helpful discussion. The authors thank the reviewers and editor for constructive feedback.

This study was supported by the NASA Astrobiology Institute (NNA13AA94A) at UW–Madison. The WiscSIMS Lab was supported by NSF (EAR–1355590, –1658823, –2004618) and UW–Madison. JWV was also supported by NSF (EAR–1524336) and DOE (DE–FG02–93ER14389). SX was supported by NASA Exobiology Program (80NSSC18K1086). HC acknowledges joint support from the CIFAR

(Canadian Institute for Advanced Research) “Earth 4D: Subsurface Science and Exploration” program at the Université de Paris and the University of Toronto.

CONFLICT OF INTERESTS

The authors declare that they have no known competing financial interests or personal relationships that could have appeared to influence the work reported in this paper

CONTRIBUTIONS

HC designed research; HC and SX conducted field work; HC and MJS prepared SIMS samples; HC and IJO performed SIMS analysis at JWV’s WiscSIMS laboratory; HC and JHF performed SEM and EPMA analyses; IJO, KK, AD, and HC corrected raw SIMS data; HC and JMB performed CL analysis; HC interpreted the results and wrote the manuscript with contributions from all coauthors. All authors contributed to discussion and manuscript revision.

ABBREVIATIONS

BSE = backscattered electron; Cal = calcite; CL = cathodoluminescence; Dol = dolomite; EN = Ediacaran negative excursion; EP = Ediacaran positive excursion; EPMA = electron probe microanalysis; GS–IRMS = gas source–isotope ratio mass spectrometry; PPL = plane polarized light; SE in text = Shuram excursion; SE in SEM images = secondary electron; SEM = scanning electron microscope; SIMS = secondary ion mass spectrometry; μXRF = micro X-ray fluorescence; VCDT = Vienna Canyon Diablo Troilite; VPDB = Vienna Pee Dee Belemnite; XRD = X-ray diffraction

APPENDICES

Appendix 1: Integrated SEM–CL–SIMS results of sample 12ZL-49.8a (PowerPoint slides)

https://dl.ipgp.fr/23li9dtk

Appendix 2: Integrated SEM–CL–SIMS results of sample 12ZL-49.8b (PowerPoint slides)

https://dl.ipgp.fr/q4f9

Appendix 3: SEM-EDS results of samples 12ZL-49.8a and 12ZL-49.8b (PowerPoint slides)

https://dl.ipgp.fr/3jvt9

Appendix 4: SIMS data (Excel spreadsheet) https://dl.ipgp.fr/y5d11r4m

Appendix 5: EPMA data (Excel spreadsheet) https://dl.ipgp.fr/59p0m

569 **TABLES 1–5**

570 **Table 1.** A summary of the analyzed SIMS spots during WiscSIMS session 2018–02–05. All data are new
571 in this study.

SIMS mount	Lithology	SIMS domain	Spot ID	CL–SEM–SIMS results
12ZL-49.8a (Fig. 6)	Dolostone partially replaced by ^{13}C-depleted authigenic calcite and a trace amount of authigenic quartz	Domain 1	@182 to @221	Fig. 13; Appendix 1
		Domain 2	@226 to @265	Fig. 14; Appendix 2
12ZL-49.8b (Fig. 7)		Domain 1	@498 to @527	Fig. 15; Appendix 3

572

573

574 **Table 2.** XRD and geochemical results of micro-drilled powders of dolostone slab12ZL-49.8. This sample
575 was collected from the upper Doushantuo Formation at the outer shelf Zhongling section, South China. The
576 stratigraphic height of this sample is 209.2 m. Micro-drilled powders was collected by using a drill bit of
577 800 μm in diameter. $\delta^{13}C$ and $\delta^{18}O$ data were analyzed by conventional GS–IRMS. XRD and geochemical
578 data are from Cui et al. (2017). Laminae 2 and 3, 5 and 6 were newly investigated by integrated μXRF–
579 SEM–CL–SIMS in this study. Abbreviations: XRD = X-ray diffraction; GS–IRMS = gas source–isotope
580 ratio mass spectrometry.

Dolostone slab 12ZL-49.8	XRD data of micro-drilled powders (Fig. 3)			GS-IRMS data of micro-drilled powders (Fig. 3)		Description	SIMS epoxy mounts (25-mm in diameter) investigated in this study
	Calcite (wt%)	Dolomite (wt%)	Quartz (wt%)	$\delta^{13}C$ (VPDB ‰)	$\delta^{18}O$ (VPDB ‰)		
Lamina 1	0.00	99.80	0.20	2.8	–5.3	Dominated by dolomite	
Lamina 2	3.24	95.83	0.93	1.9	–6.3	Dominated by dolomite	Upper half of 12ZL-49.8a (Fig. 6)
Lamina 3	39.12	59.81	1.07	–8.4	–7.2	Rich in authigenic calcite cements	Lower half of 12ZL-49.8a (Figs. 6, 13, 14)
Lamina 4	0.45	99.16	0.39	2.7	–5.8	Dominated by dolomite	
Lamina 5	0.00	99.77	0.23	2.7	–5.7	Dominated by dolomite	Upper half of 12ZL-49.8b (Fig. 7)
Lamina 6	30.61	68.33	1.05	–8.8	–7.3	Rich in authigenic calcite cements	Lower half of 12ZL-49.8b (Figs. 7, 15)
Lamina 7	0.40	99.38	0.22	2.6	–5.7	Dominated by dolomite	
Lamina 8	29.92	69.09	0.98	–10.5	–7.4	Rich in authigenic calcite cements	
Lamina 9	0.04	99.69	0.27	2.8	–5.3	Dominated by dolomite	
Lamina 10	97.10	2.50	0.34	–34.1	–9.8	Calcite nodule	

581

582 **Table 3.** SIMS and EPMA data of calcite from upper Doushantuo Formation, outer shelf Zhongling section,
583 Hunan Province, South China. Each analyzed SIMS pit has a unique spot ID that can be retrieved in the
584 online supplementary materials. Elemental concentration data of each SIMS pit were obtained based on the
585 EPMA analyses of two or three spots that are close to the SIMS pit. An averaged Fe# value = [molar ratio
586 of Fe/(Fe+Mg)] of two or three EMPA spots closely associated with each SIMS pit was used for the $\delta^{13}C_{carb}$
587 correction of each SIMS pit.
588

Sample	Domain	SIMS @	Mineralogy	$\delta^{13}C$ [‰, VPDB]	2SD [‰]	Fe#	$MnCO_3$ (mol %)	$FeCO_3$ (mol %)	$MgCO_3$ (mol %)	$CaCO_3$ (mol %)
12ZL-49.8a	Domain 1	@183	Calcite	–18.3	1.4	0.00	0.00	0.00	0.88	99.12
12ZL-49.8a	Domain 1	@184	Calcite	–24.0	1.4	0.00	0.00	0.00	0.88	99.12
12ZL-49.8a	Domain 1	@186	Calcite	–19.7	1.4	0.00	0.02	0.00	0.29	99.68
12ZL-49.8a	Domain 1	@187	Calcite	–12.4	1.4	0.00	0.02	0.00	0.29	99.68
12ZL-49.8a	Domain 1	@188	Calcite	–37.1	1.4	0.00	0.00	0.00	0.88	99.12
12ZL-49.8a	Domain 1	@189	Calcite	–21.9	1.4	0.00	0.00	0.00	0.88	99.12
12ZL-49.8a	Domain 1	@190	Calcite	–26.6	1.4	0.00	0.00	0.00	0.62	99.38
12ZL-49.8a	Domain 1	@191	Calcite	–26.2	1.4	0.00	0.00	0.00	0.62	99.38
12ZL-49.8a	Domain 1	@198	Calcite	–11.6	1.2	0.00	0.00	0.00	0.70	99.30
12ZL-49.8a	Domain 1	@199	Calcite	–16.6	1.2	0.00	0.00	0.00	1.69	98.31
12ZL-49.8a	Domain 1	@200	Calcite	–36.0	1.2	0.00	0.02	0.00	1.17	98.80
12ZL-49.8a	Domain 1	@201	Calcite	–36.8	1.2	0.00	0.00	0.00	0.82	99.18
12ZL-49.8a	Domain 1	@202	Calcite	–36.4	1.2	0.00	0.00	0.00	0.93	99.07
12ZL-49.8a	Domain 1	@203	Calcite	–35.2	1.2	0.00	0.00	0.00	0.63	99.37
12ZL-49.8a	Domain 1	@204	Calcite	–23.9	1.2	0.00	0.00	0.00	1.51	98.49
12ZL-49.8a	Domain 1	@205	Calcite	–31.4	1.2	0.01	0.00	0.00	0.73	99.26
12ZL-49.8a	Domain 2	@240	Calcite	–36.6	1.0	0.00	0.00	0.00	2.16	97.84
12ZL-49.8a	Domain 2	@241	Calcite	–37.5	1.0	0.00	0.00	0.00	1.03	98.97
12ZL-49.8a	Domain 2	@242	Calcite	–16.2	1.0	0.00	0.00	0.00	0.59	99.41
12ZL-49.8a	Domain 2	@243	Calcite	–26.7	1.0	0.00	0.00	0.00	0.59	99.41
12ZL-49.8a	Domain 2	@244	Calcite	–18.8	1.0	0.00	0.00	0.00	0.79	99.21
12ZL-49.8a	Domain 2	@245	Calcite	–13.9	1.0	0.00	0.01	0.00	1.15	98.85
12ZL-49.8a	Domain 2	@246	Calcite	–11.1	1.0	0.00	0.00	0.00	1.29	98.71
12ZL-49.8a	Domain 2	@247	Calcite	–27.7	1.0	0.00	0.00	0.00	3.27	96.73
12ZL-49.8a	Domain 2	@248	Calcite	–17.4	1.0	0.00	0.00	0.00	1.46	98.54
12ZL-49.8a	Domain 2	@249	Calcite	–24.9	1.0	0.00	0.00	0.00	0.87	99.13
12ZL-49.8a	Domain 2	@254	Calcite	–32.5	1.0	0.00	0.00	0.00	1.83	98.17
12ZL-49.8a	Domain 2	@255	Calcite	–21.8	1.0	0.00	0.00	0.00	0.75	99.25
12ZL-49.8a	Domain 2	@256	Calcite	–14.9	1.0	0.00	0.00	0.00	0.94	99.06
12ZL-49.8a	Domain 2	@257	Calcite	–23.4	1.0	0.00	0.01	0.00	0.68	99.31
12ZL-49.8a	Domain 2	@258	Calcite	–23.9	1.0	0.00	0.02	0.00	1.08	98.90
12ZL-49.8a	Domain 2	@259	Calcite	–11.0	1.0					

12ZL-49.8a	Domain 2	@260	Calcite	–14.9	1.0					
12ZL-49.8a	Domain 2	@261	Calcite	–29.1	1.0	0.00	0.00	0.00	1.77	98.23
12ZL-49.8a	Domain 2	@262	Calcite	–26.9	1.0	0.00	0.00	0.00	0.77	99.23
12ZL-49.8a	Domain 2	@263	Calcite	–12.6	1.0	0.00	0.00	0.00	1.56	98.44
12ZL-49.8a	Domain 2	@265	Calcite	–28.7	1.0	0.00	0.01	0.01	1.22	98.77
12ZL-49.8b	Domain 1	@499	Calcite	–29.3	1.0	0.00	0.00	0.00	1.50	98.50
12ZL-49.8b	Domain 1	@500	Calcite	–9.3	1.0	0.00	0.02	0.00	0.71	99.27
12ZL-49.8b	Domain 1	@501	Calcite	–19.8	1.0	0.00	0.00	0.00	1.40	98.60
12ZL-49.8b	Domain 1	@502	Calcite	–26.0	1.0	0.00	0.00	0.00	0.70	99.30
12ZL-49.8b	Domain 1	@503	Calcite	–18.7	1.0	0.00	0.00	0.00	1.04	98.96
12ZL-49.8b	Domain 1	@504	Calcite	–24.2	1.0	0.00	0.00	0.00	1.15	98.85
12ZL-49.8b	Domain 1	@505	Calcite	–15.1	1.0	0.00	0.00	0.00	2.96	97.04
12ZL-49.8b	Domain 1	@506	Calcite	–20.5	1.0	0.02	0.01	0.02	0.65	99.33
12ZL-49.8b	Domain 1	@507	Calcite	–36.6	1.0	0.00	0.00	0.00	0.87	99.13
12ZL-49.8b	Domain 1	@508	Calcite	–17.3	1.0	0.00	0.00	0.00	0.87	99.13
12ZL-49.8b	Domain 1	@509	Calcite	–37.2	1.0	0.00	0.00	0.00	0.70	99.30
12ZL-49.8b	Domain 1	@510	Calcite	–17.8	1.0	0.00	0.00	0.00	0.75	99.25
12ZL-49.8b	Domain 1	@516	Calcite	–11.9	1.0	0.00	0.01	0.00	1.51	98.49
12ZL-49.8b	Domain 1	@517	Calcite	–12.3	1.0	0.00	0.00	0.00	0.67	99.33
12ZL-49.8b	Domain 1	@518	Calcite	–31.6	1.0	0.01	0.02	0.01	0.95	99.03
12ZL-49.8b	Domain 1	@519	Calcite	–15.0	1.0	0.00	0.02	0.00	1.42	98.55
12ZL-49.8b	Domain 1	@520	Calcite	–24.0	1.0	0.00	0.00	0.00	0.73	99.27

589

590
591

Table 4. SIMS and EPMA data of dolomite from upper Doushantuo Formation, outer shelf Zhongling section, Hunan Province, South China. Each analyzed SIMS pit has a unique spot ID that can be retrieved in the online supplementary materials. Elemental concentration data of each SIMS pit were obtained based on the EPMA analyses of two or three spots that are close to the SIMS pit. An averaged Fe# value = [molar ratio of Fe/(Fe+Mg)] of two or three EMPA spots closely associated with each SIMS pit was used for the $\delta^{13}C_{carb}$ correction of each SIMS pit.

Sample	Domain	SIMS @	Mineralogy	$\delta^{13}C$ [‰, VPDB]	2SD [‰]	Bias [‰]	Fe#	$MnCO_3$ (mol %)	$FeCO_3$ (mol %)	$MgCO_3$ (mol %)	$CaCO_3$ (mol %)
12ZL-49.8a	Domain 1	@206	Dolomite	2.7	1.2	–58.9	0.00	0.00	0.00	48.25	51.75
12ZL-49.8a	Domain 1	@207	Dolomite	4.0	1.2	–58.9	0.00	0.01	0.00	48.55	51.43
12ZL-49.8a	Domain 1	@212	Dolomite	1.8	1.1	–58.7	0.00	0.00	0.03	48.71	51.25
12ZL-49.8a	Domain 1	@213	Dolomite	3.3	1.1	–58.7	0.00	0.00	0.00	48.36	51.64
12ZL-49.8a	Domain 1	@214	Dolomite	2.5	1.1	–58.7	0.00	0.00	0.06	48.63	51.31
12ZL-49.8a	Domain 1	@215	Dolomite	1.6	1.1	–58.7	0.00	0.01	0.00	49.34	50.65
12ZL-49.8a	Domain 1	@216	Dolomite	2.3	1.1	–58.7	0.00	0.00	0.04	48.60	51.36
12ZL-49.8a	Domain 1	@217	Dolomite	2.5	1.1	–58.7	0.00	0.00	0.00	48.13	51.87
12ZL-49.8a	Domain 1	@218	Dolomite	0.6	1.1	–58.7	0.00	0.00	0.00	48.68	51.32
12ZL-49.8a	Domain 1	@220	Dolomite	1.7	1.1	–58.7	0.00	0.01	0.02	48.20	51.77
12ZL-49.8a	Domain 1	@221	Dolomite	2.4	1.1	–58.7	0.00	0.00	0.00	48.65	51.34
12ZL-49.8a	Domain 2	@227	Dolomite	1.6	1.0	–58.7	0.00	0.00	0.01	48.50	51.49
12ZL-49.8a	Domain 2	@228	Dolomite	3.6	1.0	–58.6	0.00	0.00	0.00	48.72	51.28
12ZL-49.8a	Domain 2	@229	Dolomite	0.7	1.0	–58.7	0.00	0.00	0.02	48.84	51.14
12ZL-49.8a	Domain 2	@230	Dolomite	1.2	1.0	–58.7	0.00	0.00	0.02	48.59	51.39
12ZL-49.8a	Domain 2	@231	Dolomite	3.3	1.0	–58.7	0.00	0.00	0.03	48.19	51.78
12ZL-49.8a	Domain 2	@232	Dolomite	2.3	1.0	–58.6	0.00	0.00	0.00	50.11	49.89
12ZL-49.8a	Domain 2	@233	Dolomite	3.7	1.0	–58.7	0.00	0.00	0.03	48.20	51.77
12ZL-49.8a	Domain 2	@234	Dolomite	2.9	1.0	–58.6	0.00	0.00	0.00	49.30	50.70
12ZL-49.8b	Domain 2	@498	Dolomite	1.8	1.0	–58.5	0.00	0.00	0.01	48.44	51.55
12ZL-49.8b	Domain 2	@521	Dolomite	–1.5	1.0	–58.8	0.00	0.01	0.07	48.09	51.84
12ZL-49.8b	Domain 2	@522	Dolomite	0.2	1.0	–58.8	0.00	0.00	0.07	48.24	51.69
12ZL-49.8b	Domain 2	@523	Dolomite	2.2	1.0	–58.7	0.00	0.00	0.02	47.18	52.79
12ZL-49.8b	Domain 2	@524	Dolomite	1.8	1.0	–58.7	0.00	0.01	0.03	48.42	51.54
12ZL-49.8b	Domain 2	@525	Dolomite	2.0	1.0	–58.7	0.00	0.00	0.04	48.09	51.87

Table 5. A summary of the CL–SEM–SIMS results analyzed from both calcite and dolomite in the upper Doushantuo Formation, South China. The 2SD represents two standard deviations of each SIMS data set (note: not the analytical precision). The value n represents the number of analyzed SIMS spots. Data source: Jiulongwan SIMS data (Cui et al., 2021); Zhongling SIMS data (this study).

Upper Doushantuo sections	Mineral	CL	SEM petrography		SIMS $\delta^{13}C$ data (VPDB, ‰)					Interpretations	
			Texture	Grain size	Minimum	Maximum	Mean	2SD	n	Paragenesis	Carbon source
Zhongling (outer shelf environment)	Dolomite	Red and green	Homogeneous, subhedral	ca. 30 μm	–1.5	+4.0	+2.0	2.29	25	Syndeposition, early diagenesis	Open marine DIC
	Calcite	Dull	Homogeneous, subhedral	Irregular	–37.5	–9.3	–23.2	16.08	54	Early diagenesis	Methane-derived alkalinity in porewater of shallow marine sediments
Jiulongwan (intra shelf environment)	Calcite	Relative uniform	Homogeneous microspar, interlocking boundary	ca. 5–10 μm	–9.5	–6.2	–8.2	1.51	36	Deposition	Seawater DIC mixed with methane-derived alkalinity in water column of a restricted basin
	Dolomite	Zoned in dolomitic limestones	Zoned, often with irregular boundary in dolomitic limestones	up to 100 μm	–11.2	–3.8	–7.9	2.93	91	Post-deposition	Inherited from the preexisting calcite

611 **FIGURES 1–17**

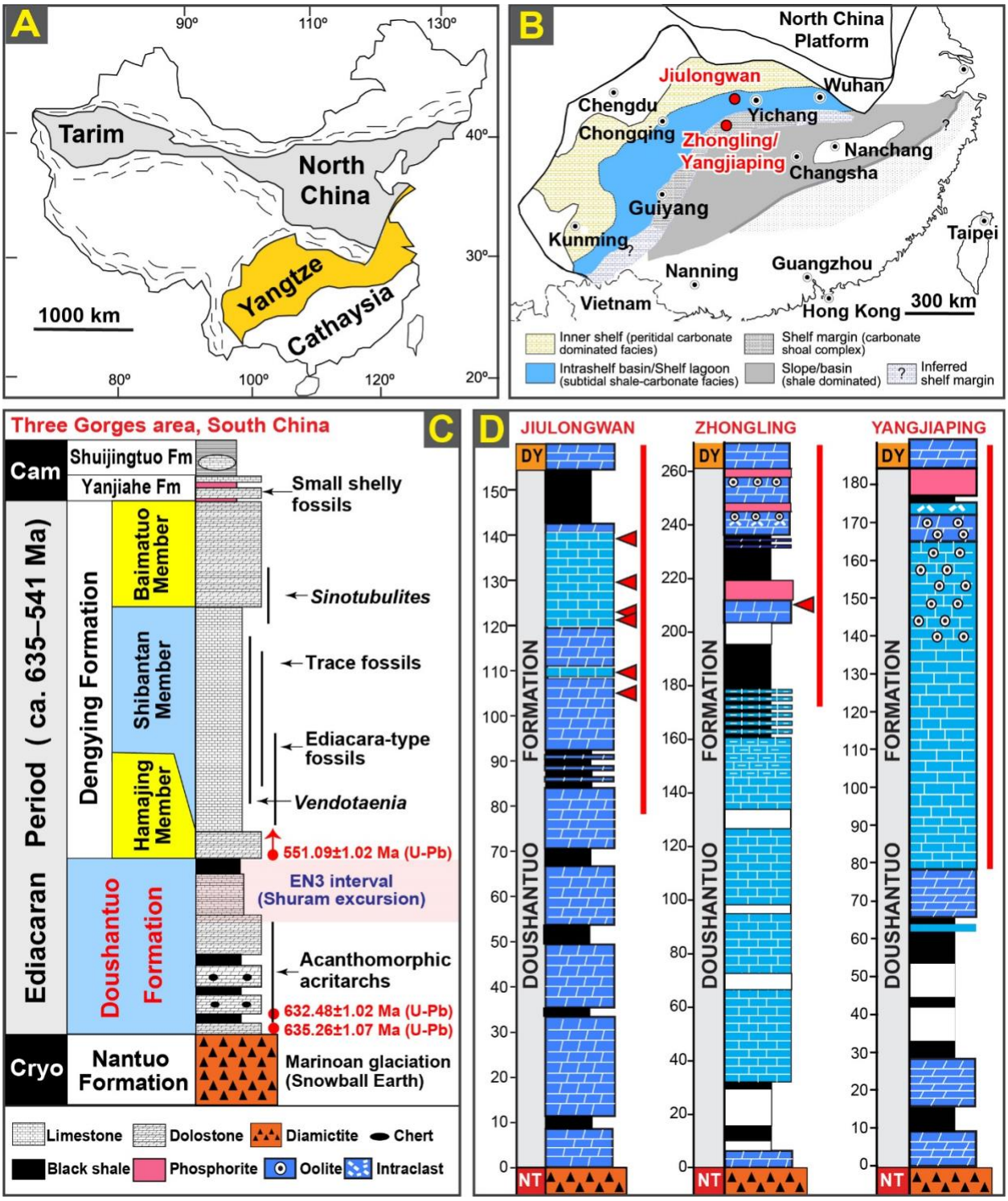

612

613 **Fig. 1. Maps and stratigraphic columns. (A)** Geological map of China, with the Yangtze Craton in yellow.
614 **(B)** Reconstructed Ediacaran depositional environments on the Yangtze Craton (Jiang et al., 2011). Red
615 dots indicate the locations of the Jiulongwan (intra shelf) and Zhongling/Yangjiaping (outer shelf) sections.

(C) Simplified litho-, bio-, and chrono-stratigraphy of the Ediacaran Doushantuo and Dengying formations in South China. Thickness is not to scale. Note that the 551 Ma age was initially placed to the Doushantuo–Dengying boundary by Condon et al. (2005), but was later re-assigned to the Shibantan Member of the Dengying Formation based on a more recent chemostratigraphic study (An et al., 2015), although it still remains a matter of debate (Zhou et al., 2017). Figure modified from Chen et al. (2013) and Cui et al. (2017). **(D)** Lithological columns of the Doushantuo Formation at the intra shelf Jiulongwan section and the outer shelf Zhongling and Yangjiaping sections. Red triangles represent horizons analyzed by SIMS (Cui et al., 2021; this study). Red bars represent the intervals shown in Fig. 2. Radiometric ages from Condon et al. (2005) and Schmitz (2012). Abbreviations used: Cam = Cambrian; Cryo = Cryogenian; DY = Dengying; NT = Nantuo.

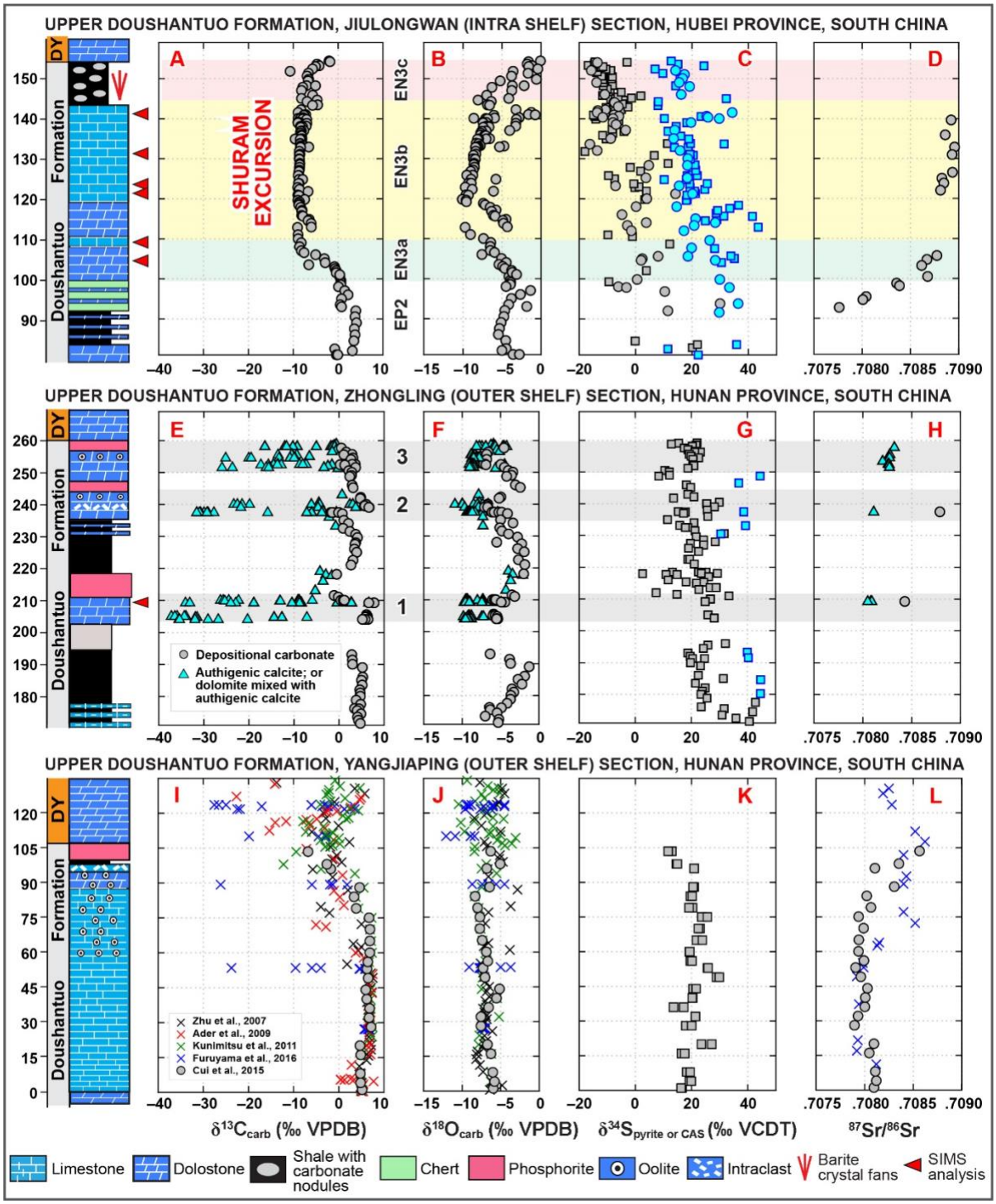

Fig. 2. Chemostratigraphic profiles of the upper Doushantuo Formation at the intra shelf Jiulongwan section and the outer shelf Zhongling and Yangjiaping sections. All the plotted data were measured on conventional micro-drilled bulk powders (for $\delta^{13}C_{carb}$, $\delta^{18}O_{carb}$, and $^{87}Sr/^{86}Sr$ analyses) or bulk acidified residuals (for $\delta^{34}S$ analyses). Red triangles alongside the lithological columns of the Jiulongwan and Zhongling sections represent the horizons investigated by SIMS (Cui et al., 2021; this study). **(A, E, I)** $\delta^{13}C_{carb}$ (‰, VPDB)

profiles. Green-, yellow-, and red-shaded intervals of the Jiulongwan section represent EN3a, EN3b, and EN3c, respectively, which are defined by McFadden et al. (2008). The three gray-shaded intervals at Zhongling show intervals with highly negative $\delta^{13}C_{carb}$ in authigenic calcite, suggesting pulsed occurrence of methane oxidation (Cui et al., 2017). A thorough investigation was also conducted for the lower 200 meters of the Zhongling section, but no methane-derived authigenic calcite was found. **(B, F, J)** $\delta^{18}O_{carb}$ (‰, VPDB). **(C, G, K)** $\delta^{34}S_{pyrite}$ (‰, VCDT, gray color) and $\delta^{34}S_{CAS}$ (‰, VCDT, cyan color). **(D, H, L)** $^{87}Sr/^{86}Sr$ of carbonates. Triangles in **E, F,** and **H** represent micro-drilled authigenic calcite or micro-drilled dolomite matrix mixed with various amounts of authigenic calcite cements. Data sources: Jiulongwan $\delta^{13}C_{carb}$, $\delta^{18}O_{carb}$ (McFadden et al., 2008); Jiulongwan $\delta^{34}S_{pyrite}$ shown as squares (McFadden et al., 2008); Jiulongwan $\delta^{34}S_{pyrite}$ shown as circles (Shi et al., 2018); Jiulongwan $^{87}Sr/^{86}Sr$ (Sawaki et al., 2010); All the Zhongling data (Cui et al., 2017); Yangjiaping data shown as circles and squares (Cui et al., 2015); Yangjiaping data shown as X (Zhu et al., 2007b; Ader et al., 2009; Kunimitsu et al., 2011; Furuyama et al., 2016). Abbreviations: EN = Ediacaran negative excursion ; EP = Ediacaran positive excursion; CAS = carbonate-associated sulfate; DY = Dengying.

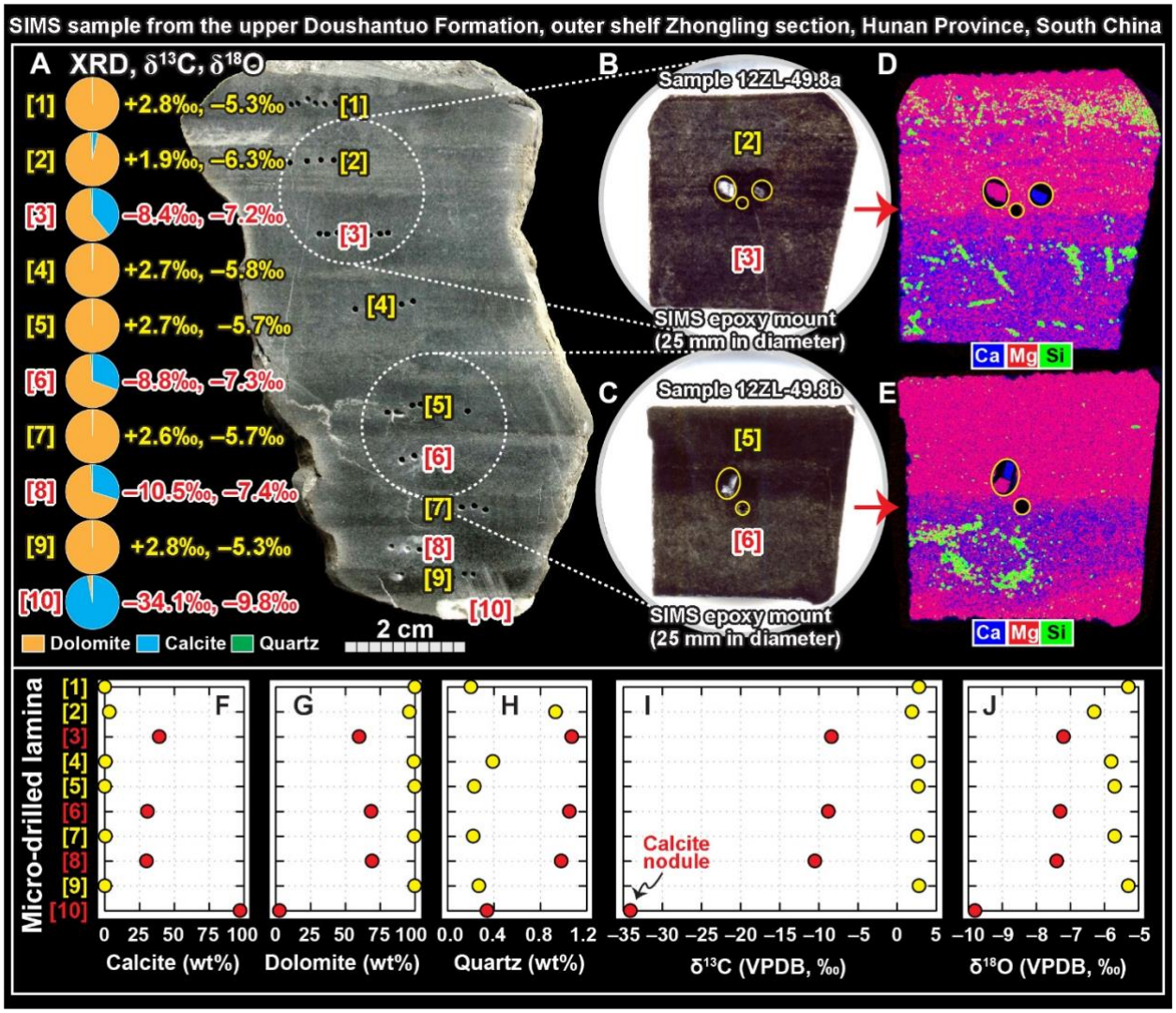

Fig. 3. Laminated dolostone sample 12ZL–49.8 investigated in this study by SEM–CL–μXRF–SIMS. This sample was collected from the upper Doushantuo Formation (209.2 m in height) at the outer shelf Zhongling section, Hunan Province, South China. **(A)** Photograph of the analyzed sample (12ZL–49.8). Yellow (indicating dolomite-rich) and red (indicating calcite-rich) numbers from [1] to [10] represent ten micro-drilled laminae. $\delta^{13}C_{carb}$ and $\delta^{18}O_{carb}$ data of micro-drilled powders were analyzed by conventional GS–IRMS. Pie chart shows different proportions of calcite (blue), dolomite (orange), and quartz (green) for each sample based on the XRD data of micro-drilled powders from each lamina. Note the remarkable heterogeneity of $\delta^{13}C_{carb}$ in alternating laminae and the extremely negative $\delta^{13}C_{carb}$ value of –34.1‰ from a small white-colored calcite nodule at the bottom of this slab. **(B, C)** SIMS epoxy mounts investigated in this study. Each SIMS mount is 25 mm in diameter, with three WiscSIMS standards (calcite UWC3, dolomite UW6220, and pyrite UWPy1) mounted in the center (marked by yellow circles). Panorama views of these two SIMS mounts under BSE can be found in Figs. 6 and 7, respectively. **(D, E)** Elemental maps of Ca (blue), Mg (red), and Si (green) generated by μXRF. Note that the upper half of the SIMS mount is

662 dominated by dolomite, and has positive $\delta^{13}C_{carb}$ values; whereas the lower half of each SIMS epoxy mount
663 is rich in ^{13}C-depeted authigenic calcite and a trace amount of authigenic quartz. **(F–H)** XRD results of the
664 ten micro-drilled laminae of slab 12ZL–49.8. **(I–J)** $\delta^{13}C_{carb}$ and $\delta^{18}O_{carb}$ data of the ten microdrilled laminae
665 of slab 12ZL–49.8. Data source: GS–IRMS and XRD data (Cui et al., 2017); SIMS epoxy mounts and
666 μXRF results (this study).

667

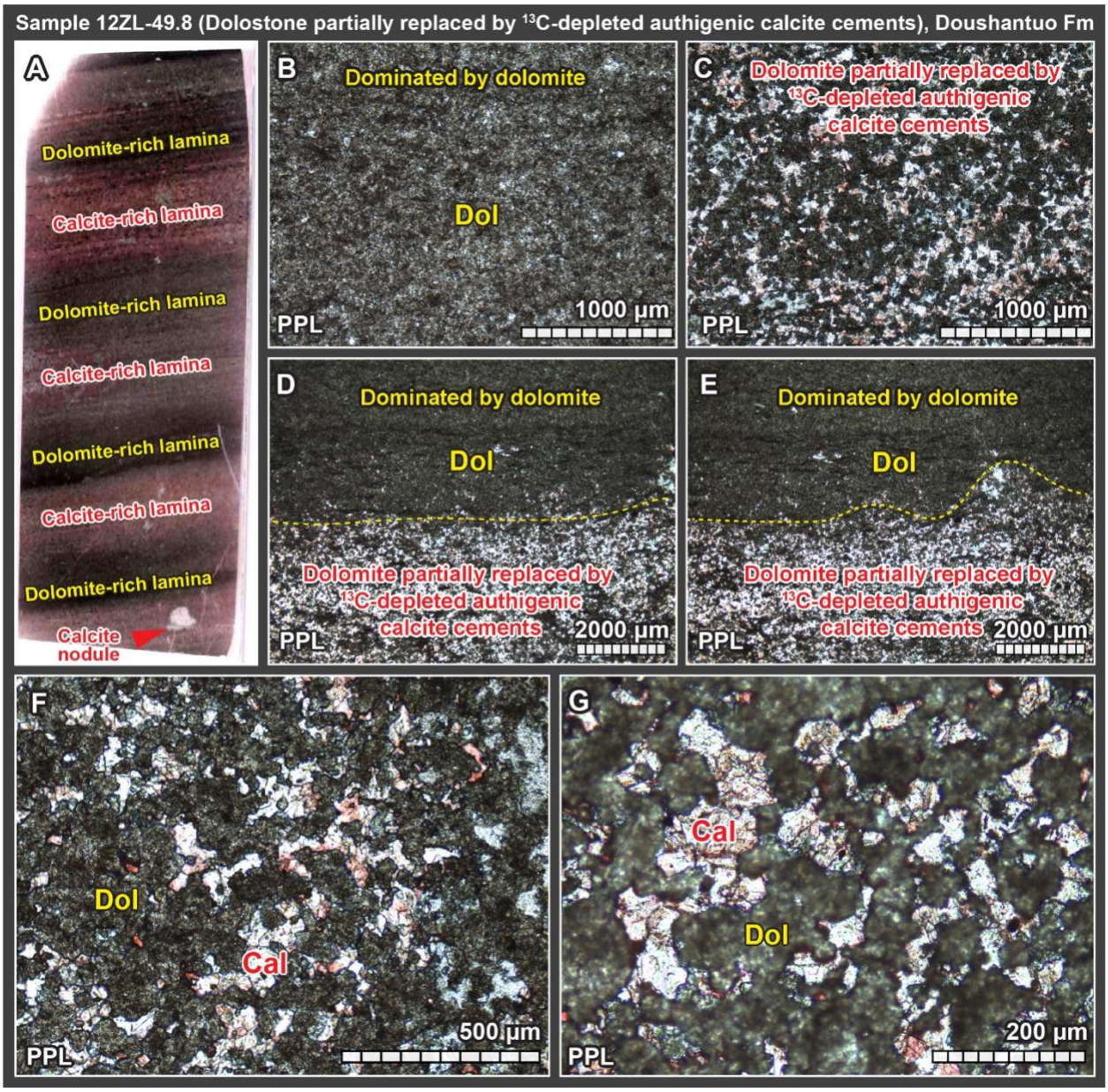

668

669 **Fig. 4.** Petrographic results under optical microscope showing the Zhongling dolostone partially replaced
670 by authigenic calcite. **(A)** Thin section slide stained by Alizarin-red S, showing interbedded authigenic-
671 calcite-rich laminae (reddish) and dolomite-dominated laminae (brownish). The width of this thin section
672 is ca. 2 cm. **(B)** Petrographic view showing lamina dominated by dolomite. **(C)** Petrographic view showing
673 dolomite partially replaced by ^{13}C-depleted authigenic calcite cements. **(D, E)** Petrographic view showing
674 the transition between dolomite-dominated lamina and authigenic-calcite-rich lamina. **(F, G)** Petrographic
675 views showing dolomite partially replaced by ^{13}C-depleted authigenic calcite cements. Abbreviations: Cal
676 = calcite; Dol = dolomite; PPL = plane polarized light.

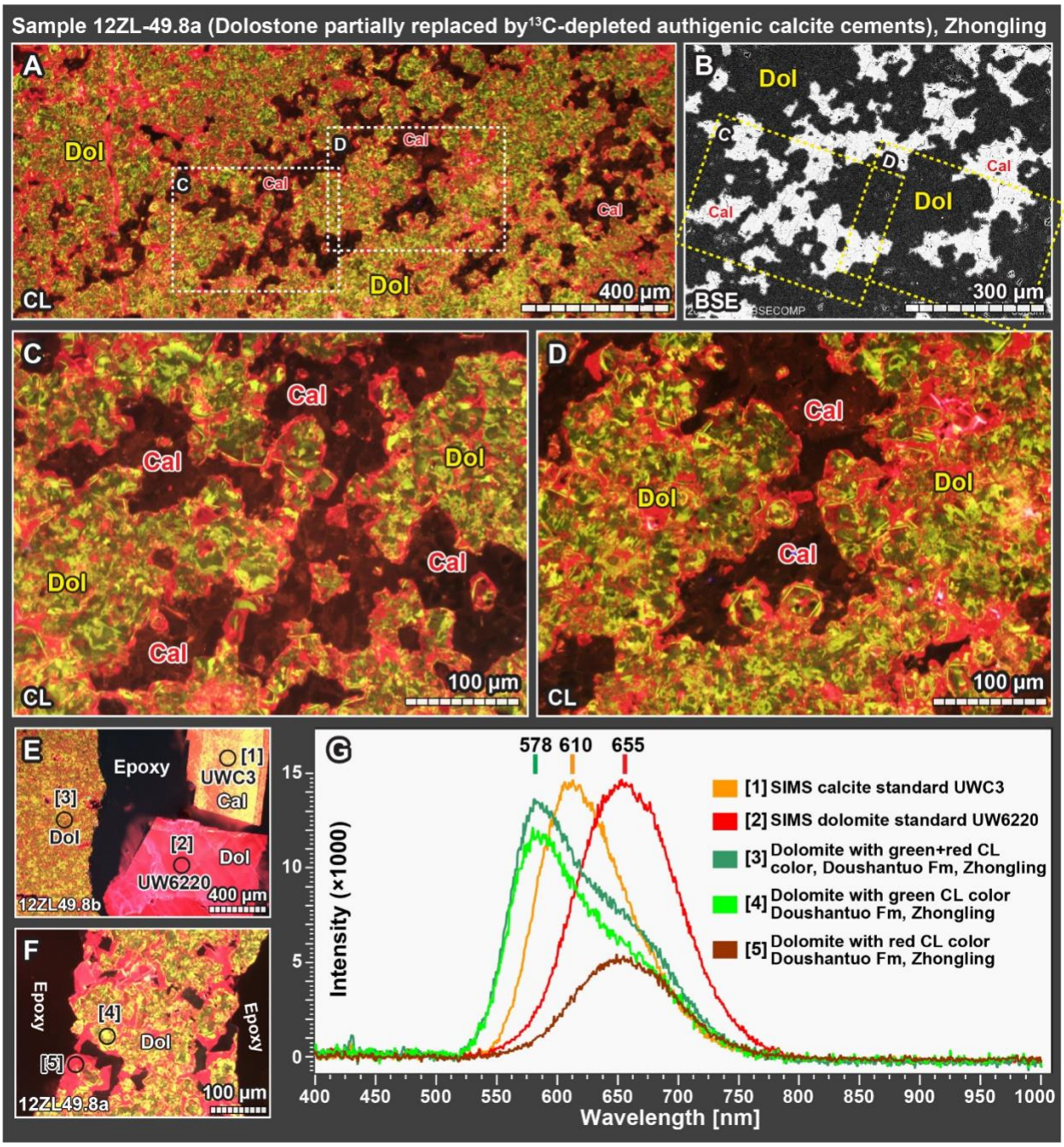

677

678 **Fig. 5.** Cathodoluminescence (CL) images and spectra analysis of the calcite and dolomite phases in sample
679 12ZL–49.8. **(A)** The dolomite matrix with positive $\delta^{13}C_{carb}$ values typically shows distinct green + red
680 luminescence, whereas the ^{13}C-depleted authigenic calcite cements typically shows dull luminescence.
681 Dash-line boxes show the same views of images C and D. **(B)** A similar view of the center part of image A
682 under BSE. Dolomicrite and ^{13}C-depleted authigenic calcite show dark and light color, respectively, under
683 BSE. **(C, D)** Closer views of the domains marked by dash-line boxes in images A and B. **(E)** CL image of
684 dolomite matrix and WiscSIMS standards (calcite UWC3, dolomite UW6220) in SIMS epoxy mount

12ZL–49.8b. Note that the calcite standard UWC3, dolomite standard UW6220, and Zhongling dolomite matrix show distinct orange, red, and a mixed green + red color, respectively. The size of analyzing spot is ~120 μm in diameter. **(F)** CL image of dolomite matrix in SIMS epoxy mount 12ZL–49.8a. The size of analyzing spot is ~30 μm in diameter. **(G)** CL spectra of the five analyzed spots. Abbreviations: BSE = backscattered electron; SE = secondary electron; SEM = scanning electron microscope; CL = cathodoluminescence; Cal = calcite; Dol = dolomite.

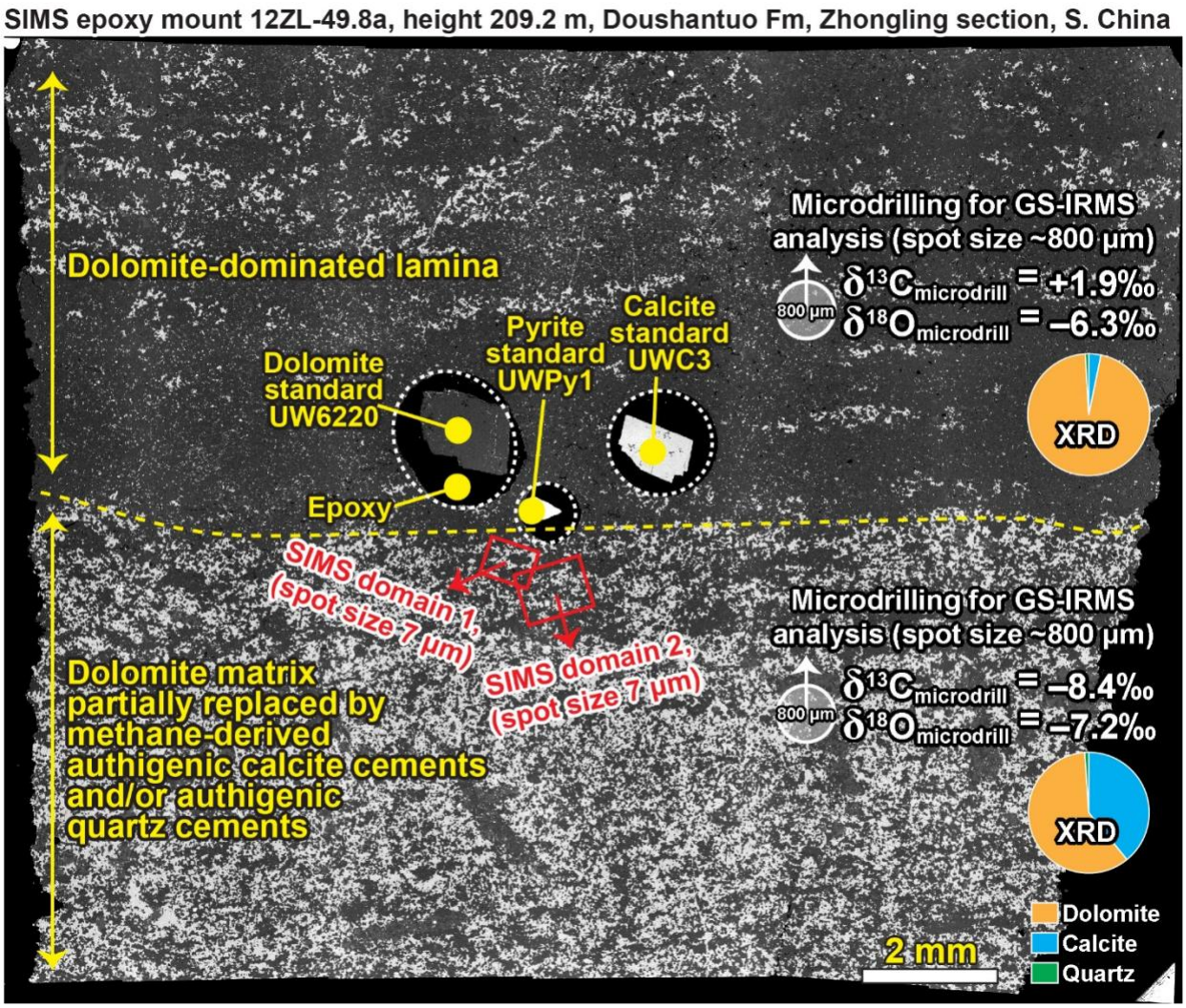

Fig. 6. Composite panorama of SIMS epoxy mount 12ZL–49.8a based on 6×6 BSE images. This SIMS mount is 25 mm in diameter, with three WiscSIMS standards (calcite UWC3, dolomite UW6220, and pyrite UWPy1) mounted in the center. The upper part is dominated by dolomite (darker under BSE), whereas the lower half shows dolomite matrix mixed with ^{13}C-depleted authigenic calcite (brighter under BSE) and a trace amount of authigenic quartz. The $\delta^{13}C_{carb}$ (V-PDB), $\delta^{18}O_{carb}$ (V-PDB), and XRD data of micro-drilled powers from the upper and lower halves were analyzed by conventional gas-source isotope ratio mass spectrometer (GS–IRMS) and provided on top of the image. Note that the spot size of micro-drilling bit is ~800 μm, while the spot size of SIMS pit in this study is 7 μm. Therefore, SIMS analysis in this study offers much higher spatial resolution than conventional GS–IRMS analysis. Data source: GS–IRMS and XRD data (Cui et al., 2017); SEM and SIMS results (this study).

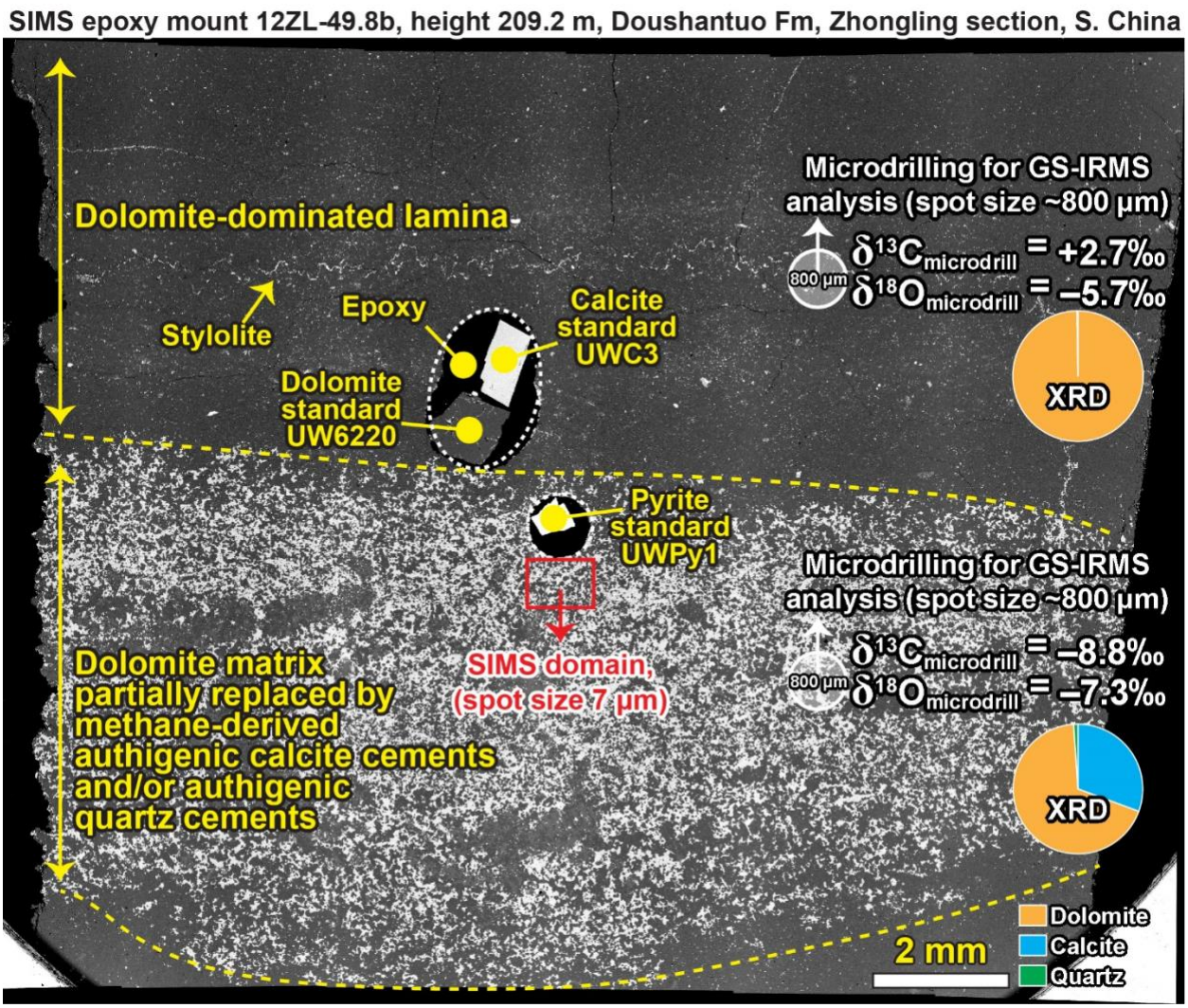

Fig. 7. Composite panorama of SIMS epoxy mount 12ZL–49.8b based on 6×6 BSE images. This SIMS mount is 25 mm in diameter, with three WiscSIMS standards (calcite UWC3, dolomite UW6220, and pyrite UWPy1) mounted in the center. The upper part is dominated by dolomite (darker under BSE), whereas the lower half shows dolomite matrix mixed with ^{13}C-depleted authigenic calcite (brighter under BSE) and a trace amount of authigenic quartz. The $\delta^{13}C_{carb}$ (V-PDB), $\delta^{18}O_{carb}$ (V-PDB), and XRD data of micro-drilled powers from the upper and lower halves were analyzed by conventional gas-source isotope ratio mass spectrometer (GS–IRMS) and provided on top of the image. Note that the spot size of micro-drilling bit is ~800 μm, while the spot size of SIMS pit in this study is 7 μm. Therefore, SIMS analysis in this study offers much higher spatial resolution than conventional GS–IRMS analysis. Data source: GS–IRMS and XRD data (Cui et al., 2017); SEM and SIMS results (this study).

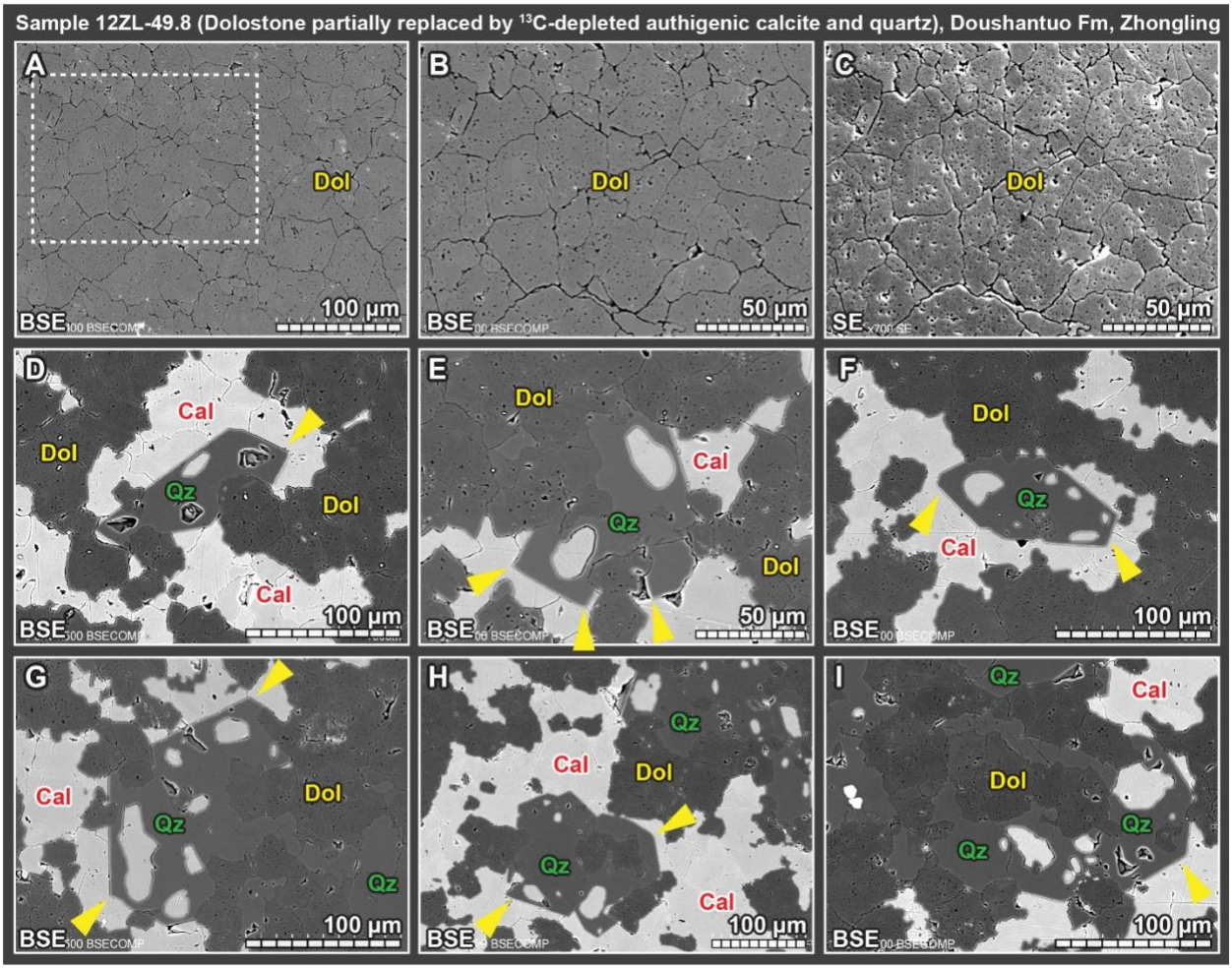

715

716 **Fig. 8.** Typical microscopic features of sample 12ZL–49.8 under SEM. **(A, B)** Dolomite matrix consisting
717 of pervasive subhedral dolomicrite with an overall grain size of ca. 30 μm. Dash-line box in A shows the
718 same view of image B. **(C)** Secondary electron image of the same view in image B. Note the interlocking
719 boundary of subhedral, inclusion-rich dolomicrite grains. **(D–I)** Dolomicrite matrix (dark color, rich in
720 inclusions on BSE) partially replaced by ^{13}C-depleted authigenic calcite (light color, free of inclusions on
721 BSE) and a trace amount of authigenic quartz (dark color, free of inclusions on BSE). Note the sharp crystal
722 terminations of authigenic quartz (yellow arrows). All images are under BSE except for the SE image in C.
723 Abbreviations: BSE = backscattered electron; SE = secondary electron; SEM = scanning electron
724 microscope; Cal = calcite; Dol = dolomite; Qz = quartz.

725

726

727

728

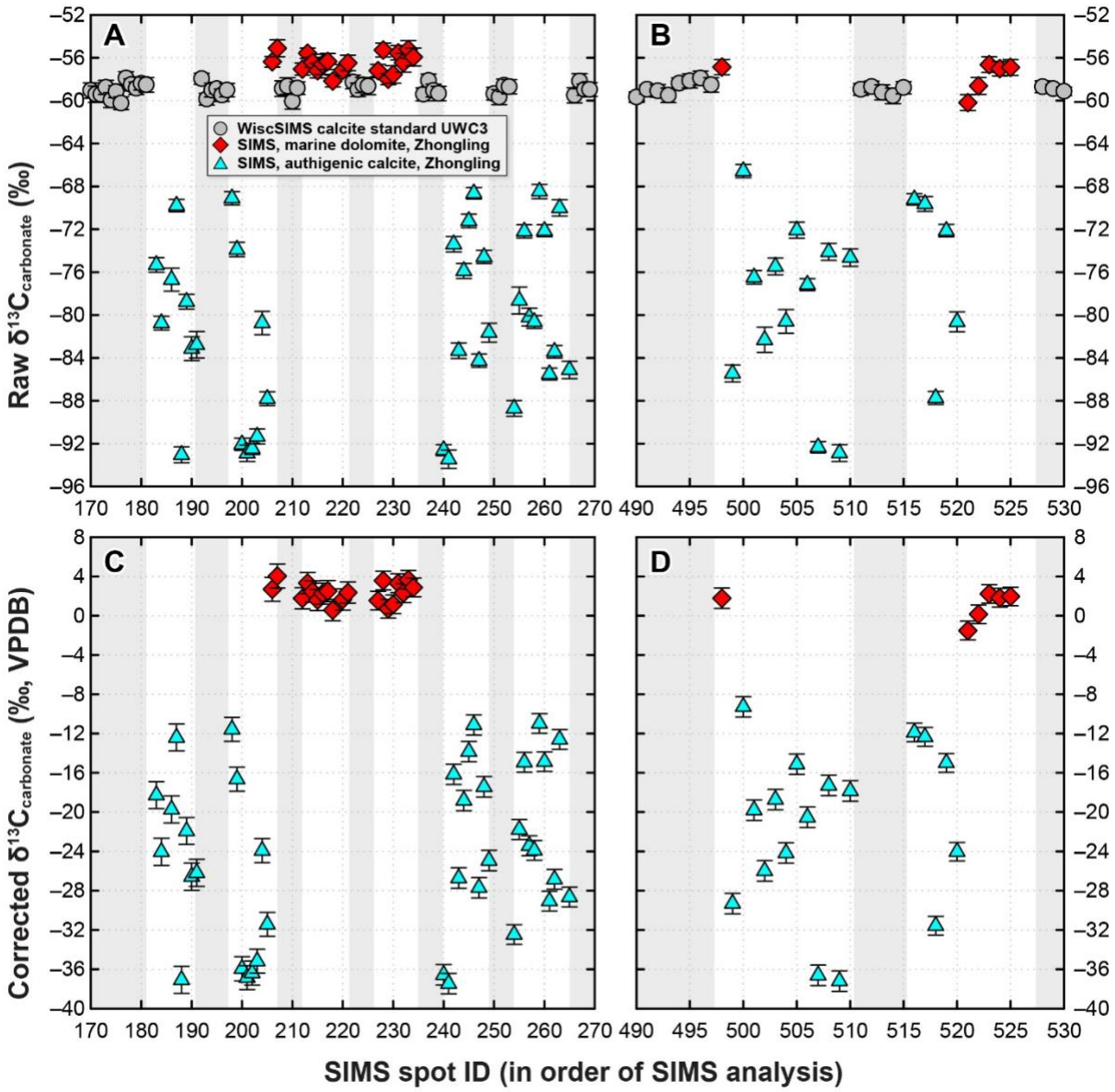

729

730 **Fig. 9. (A, B)** Raw $\delta^{13}C_{carbonate}$ data in order of SIMS analysis. **(C, D)** Corrected $\delta^{13}C_{carbonate}$ data in order of
731 SIMS analysis. The X-axis shows the unique code of each spot analysis during WiscSIMS session 2018–
732 02–05. Gray-shaded intervals represent the analyses of UWC3 calcite standard. All the data are new in this
733 study and are available in the online supplementary material.

734

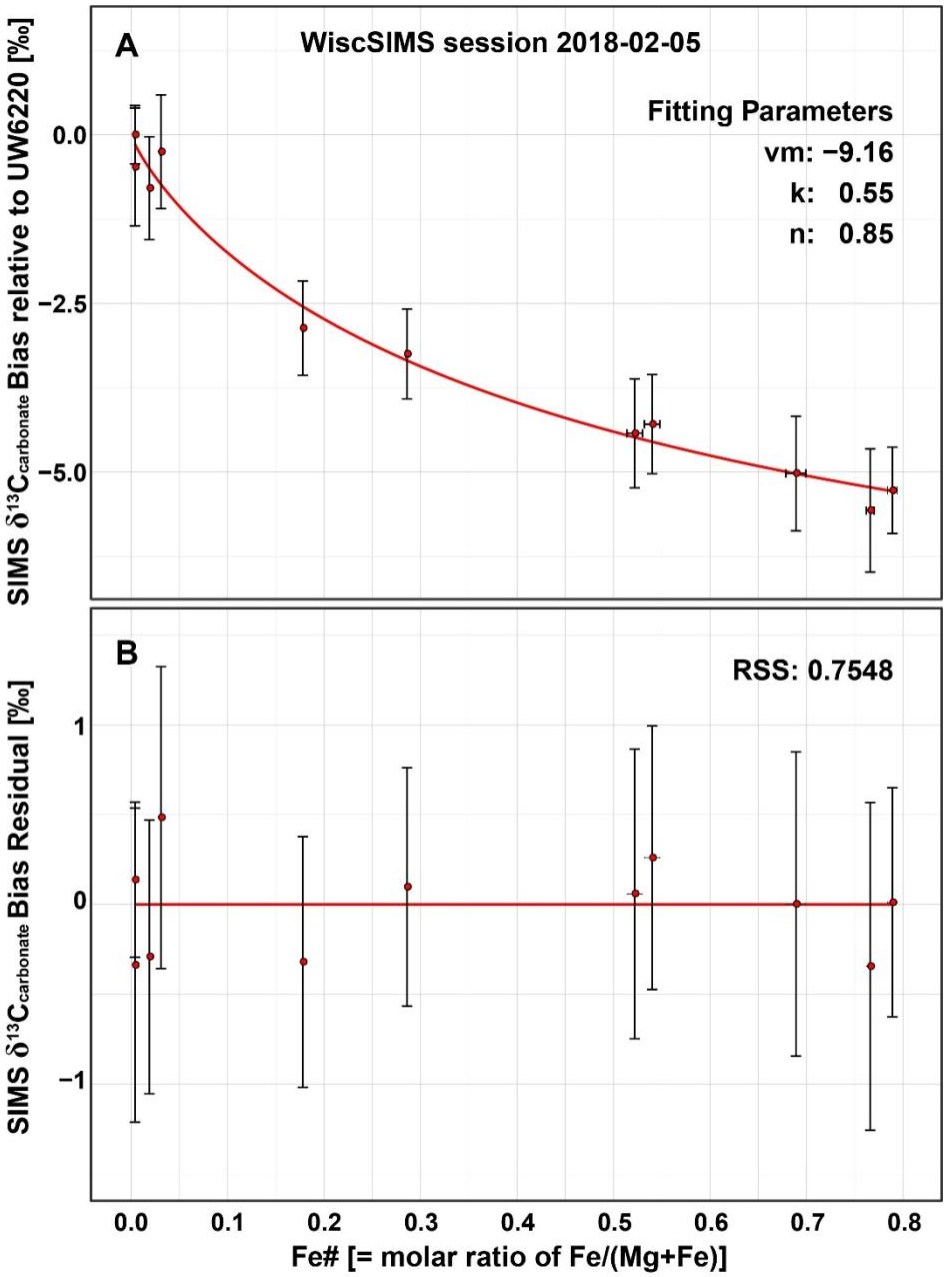

Fig. 10. SIMS $\delta^{13}C_{carbonate}$ bias or instrumental mass fractionation (IMF) during session 2018-02-05 plotted against Fe# [= molar ratio of Fe/(Mg+Fe)]. **(A)** SIMS bias relative to WiscSIMS dolomite standard UW6220. **(B)** SIMS bias residuals after correction. Error bars represent propagated errors [= (ERR_RM^2 + ERR_STD^2)^0.5] calculated from the 2SE of reference materials (i.e., calibration standards) (ERR_RM) and the 2SE of bracketing standards for calibration standards (ERR_STD).

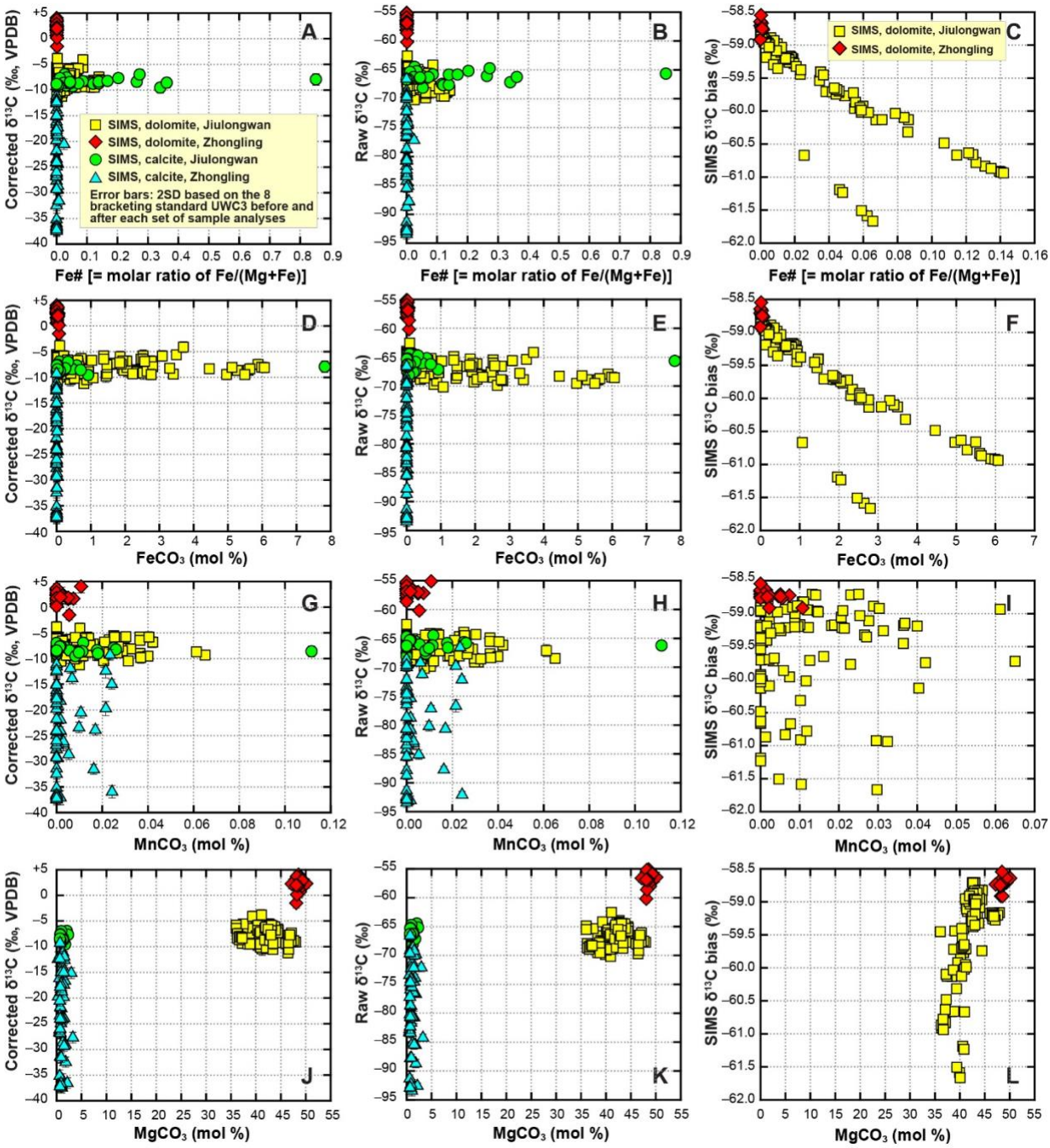

Fig. 11. Cross-plots of SIMS data vs. elemental abundances. **(A–C)** Cross-plots of the corrected SIMS data, raw SIMS data, and instrumental bias vs. Fe# [= molar ratio of Fe/(Mg+Fe)]. **(D–F)** Cross-plots of the corrected SIMS data, raw SIMS data, and instrumental bias vs. $FeCO_3$ (mol%). **(G–I)** Cross-plots of the corrected SIMS data, raw SIMS data, and instrumental bias vs. $MnCO_3$ (mol%). **(J–L)** Cross-plots of the corrected SIMS data, raw SIMS data, and instrumental bias vs. $MgCO_3$ (mol%). Note that the dolomite data from Zhongling show very low Fe#, $FeCO_3$ (mol%), and $MnCO_3$ (mol%), while the dolomite data from

Jiulongwan show much larger range and variations. Data source: Jiulongwan SIMS and EPMA data (Cui et al., 2021); Zhongling SIMS and EPMA data (this study).

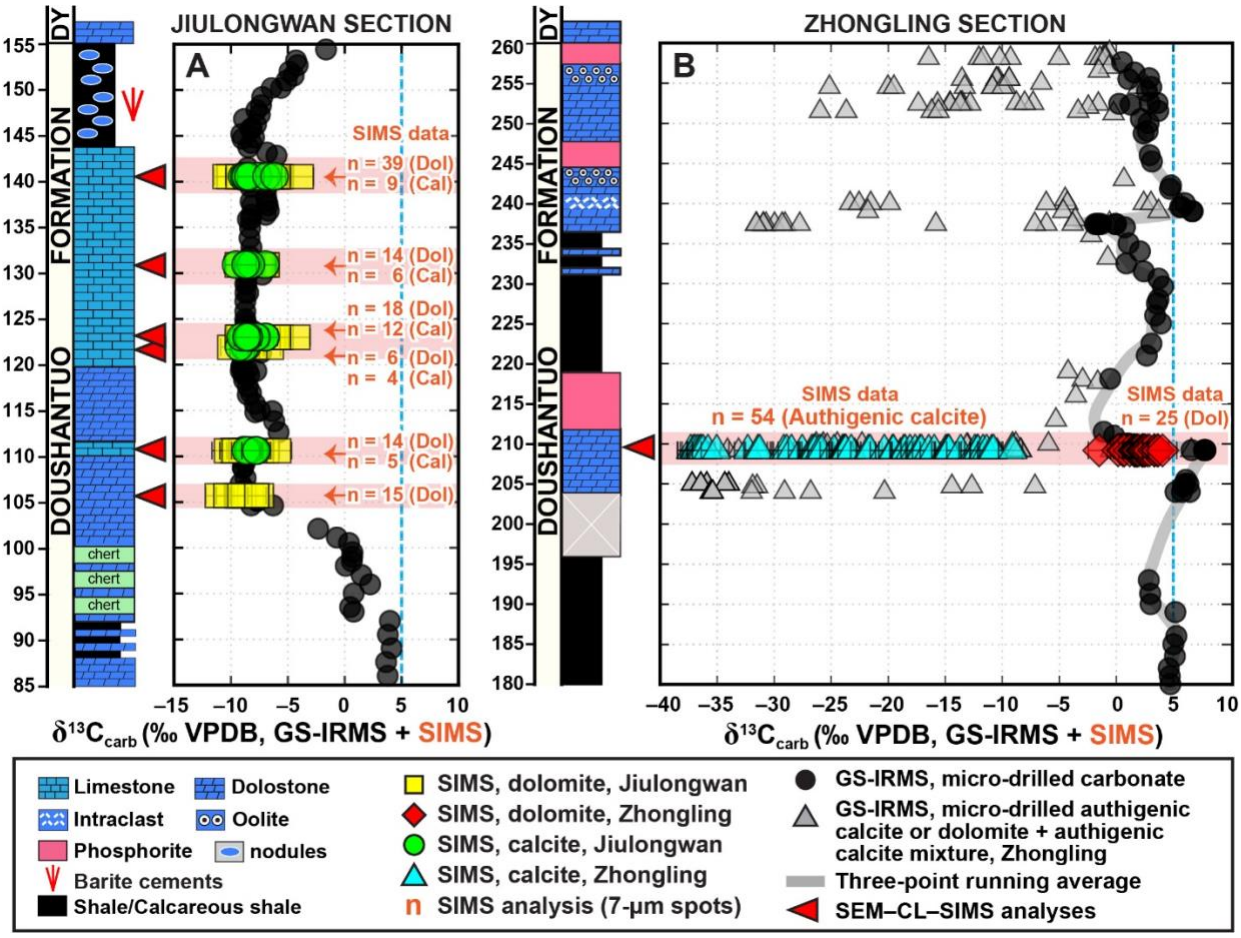

Fig. 12. Chemostratigraphic $\delta^{13}C_{carb}$ profiles of the upper Doushantuo Formation at Jiulongwan and Zhongling, South China. Red triangles alongside the lithological column at Jiulongwan and Zhongling represent the horizons investigated by SIMS (Cui et al., 2021; this study). The numbers of SIMS spots (n) analyzed in each mineral are also provided. Blue dash line ($\delta^{13}C_{carb}$ = +5‰) represents the background value of depositional carbonate of the Doushantuo Formation during the Ediacaran Period. **(A)** $\delta^{13}C_{carb}$ profile of the upper Doushantuo Formation at the intrashelf Jiulongwan section, Hubei Province, South China. **(B)** $\delta^{13}C_{carb}$ profile of the upper Doushantuo Formation at the outer shelf Zhongling section, Hunan Province, South China. Data Source: Jiulongwan micro-drilled data analyzed by GS–IRMS (McFadden et al., 2008); Jiulongwan SIMS data (Cui et al., 2021); Zhongling micro-drilled data analyzed by GS–IRMS (Cui et al., 2017); Zhongling SIMS data (this study). Abbreviations: GS–IRMS = gas-source isotope ratio mass spectrometer; SIMS = secondary ion mass spectrometer; Cal = calcite; Dol = dolomite; DY = Dengying.

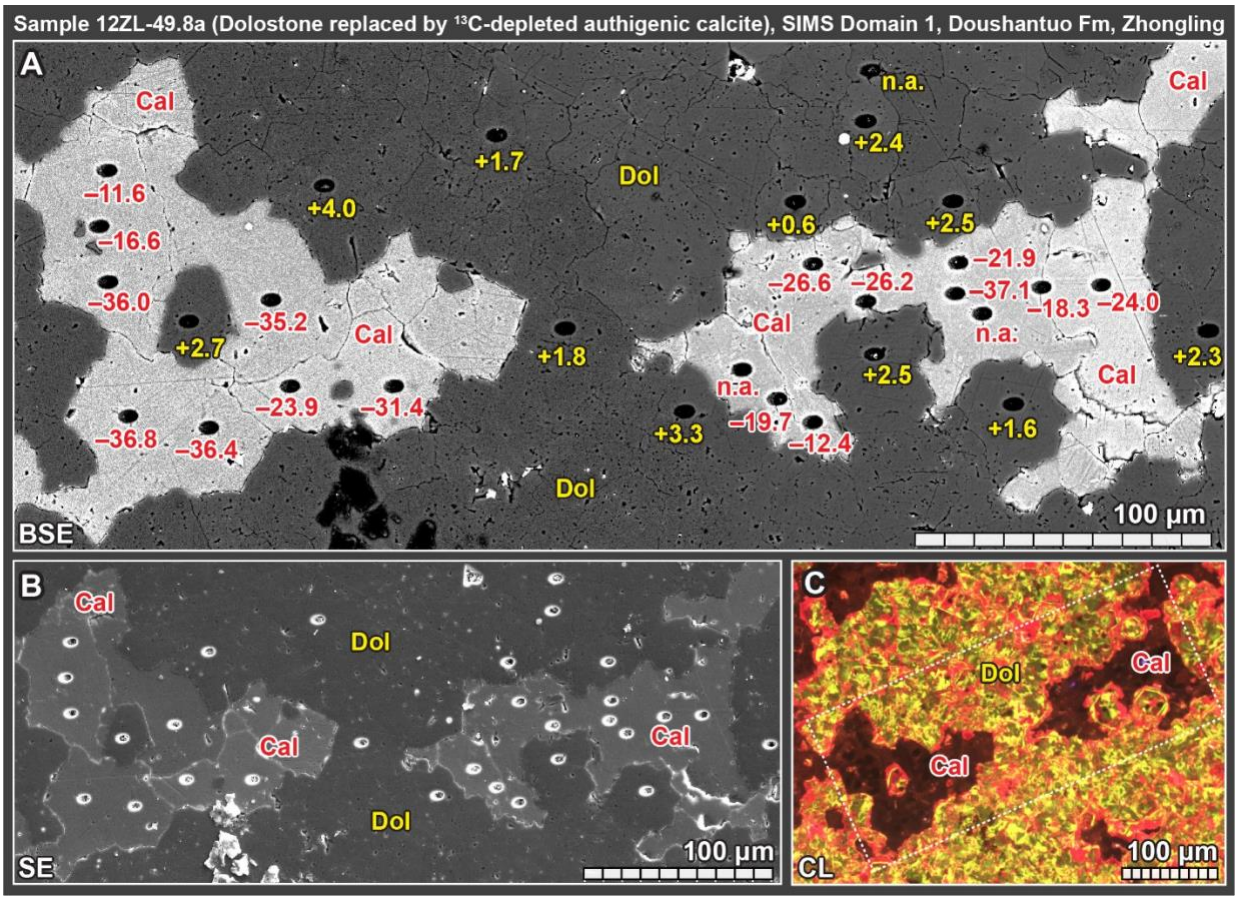

Fig. 13. Integrated SEM–CL–SIMS results of domain 1, sample 12ZL–49.8a. Values of $\delta^{13}C$ are adjacent to 7-µm SIMS pits. **(A)** BSE image with SIMS $\delta^{13}C_{calcite}$ and $\delta^{13}C_{dolomite}$ (‰, VPDB) data shown in red and yellow color, respectively. **(B)** Corresponding SE image of A. **(C)** Corresponding CL image, with the dashed box marking the same view of A and B. Note the green + red luminescence of dolomite and the overall dull luminescence of ^{13}C-depleted authigenic calcite. Abbreviations: BSE = backscattered electron; SE = secondary electron; SEM = scanning electron microscope; CL = cathodoluminescence; Cal = calcite; Dol = dolomite; Qz = quartz.

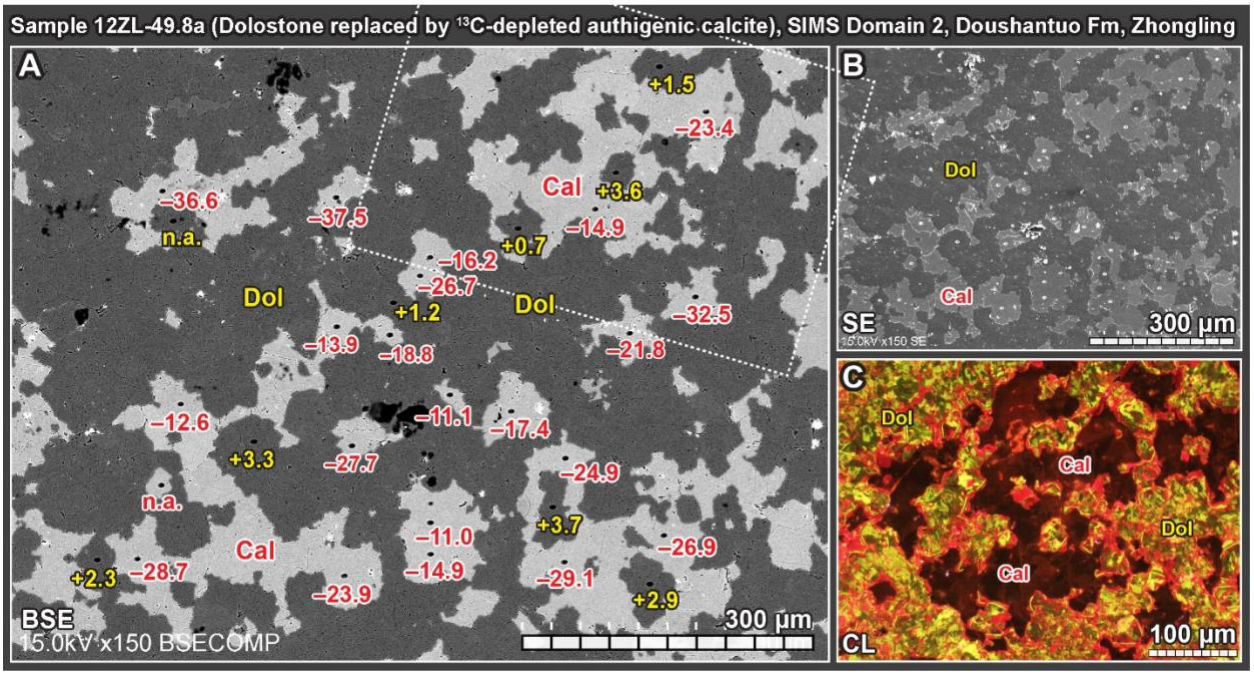

Fig. 14. Integrated SEM–CL–SIMS results of domain 2, sample 12ZL–49.8a. Values of $\delta^{13}C$ are adjacent to 7-µm SIMS pits. **(A)** BSE image with SIMS $\delta^{13}C_{calcite}$ and $\delta^{13}C_{dolomite}$ (‰, VPDB) data shown in red and yellow color, respectively. Dash-line box marks the same view of image C. **(B)** Corresponding SE image of image A. **(C)** CL image of the view marked by dash-line box in A. Note the distinct green + red luminescence of dolomite and the overall dull luminescence of ^{13}C-depleted authigenic calcite. The dashed boxes in **A–C** mark the same area. Abbreviations: BSE = backscattered electron; SE = secondary electron; SEM = scanning electron microscope; CL = cathodoluminescence; Cal = calcite; Dol = dolomite; Qz = quartz.

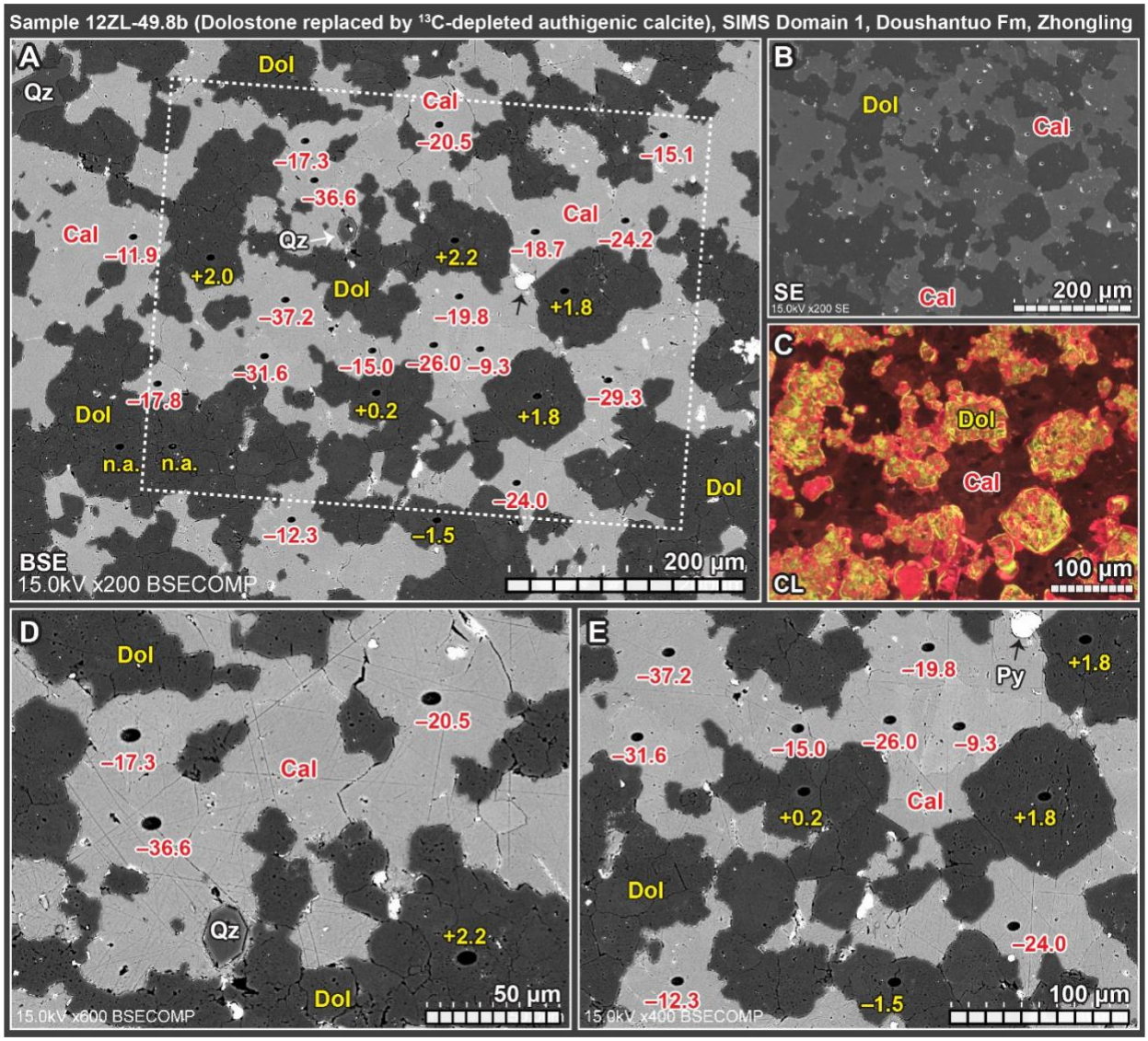

Fig. 15. Integrated SEM–CL–SIMS results of domain 1, sample 12ZL–49.8b. Values of $\delta^{13}C$ are adjacent to 7-µm SIMS pits. **(A)** BSE image with SIMS $\delta^{13}C_{calcite}$ and $\delta^{13}C_{dolomite}$ (‰, VPDB) data shown in red and yellow color, respectively. Dash-line box marks the same view of image C. **(B)** Corresponding SE image of image A. **(C)** Corresponding CL image of area marked by the dash-line box in A. Note the distinct green + red luminescence of dolomite and the overall dull luminescence of ^{13}C-depleted authigenic calcite. **(D–E)** Closer views of domains within image A. Abbreviations: BSE = backscattered electron; SE = secondary electron; SEM = scanning electron microscope; CL = cathodoluminescence; Cal = calcite; Dol = dolomite; Qz = quartz.

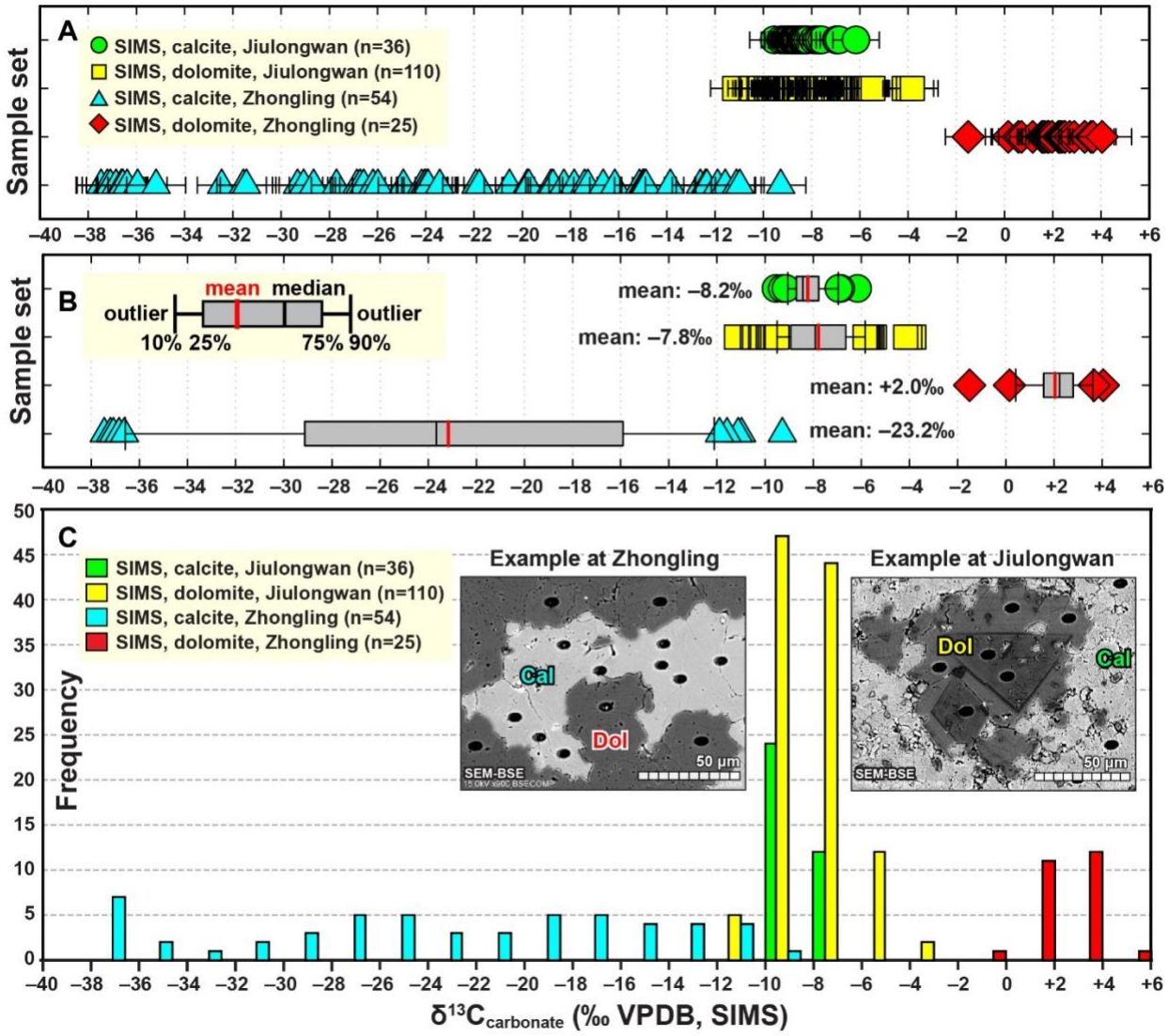

Figure 16. Summary of SIMS data. (A) Plot of each individual SIMS $\delta^{13}C_{carb}$ analysis from dolomite and calcite at the Zhongling and Jiulongwan sections. (**B**) Box plot of the SIMS $\delta^{13}C_{carb}$ data. **(C)** Histogram of the SIMS $\delta^{13}C_{carb}$ data. Note the narrow range of the Jiulongwan SIMS $\delta^{13}C_{carb}$ data and the remarkably wider range of the Zhongling SIMS $\delta^{13}C_{carb}$ data. Data Source: Jiulongwan SIMS data (Cui et al., 2021); Zhongling SIMS data (this study). Abbreviations: SIMS = secondary ion mass spectrometry; Cal = calcite; Dol = dolomite. SEM images of all the SIMS spots analyzed in this study can be found in the online supplementary materials.

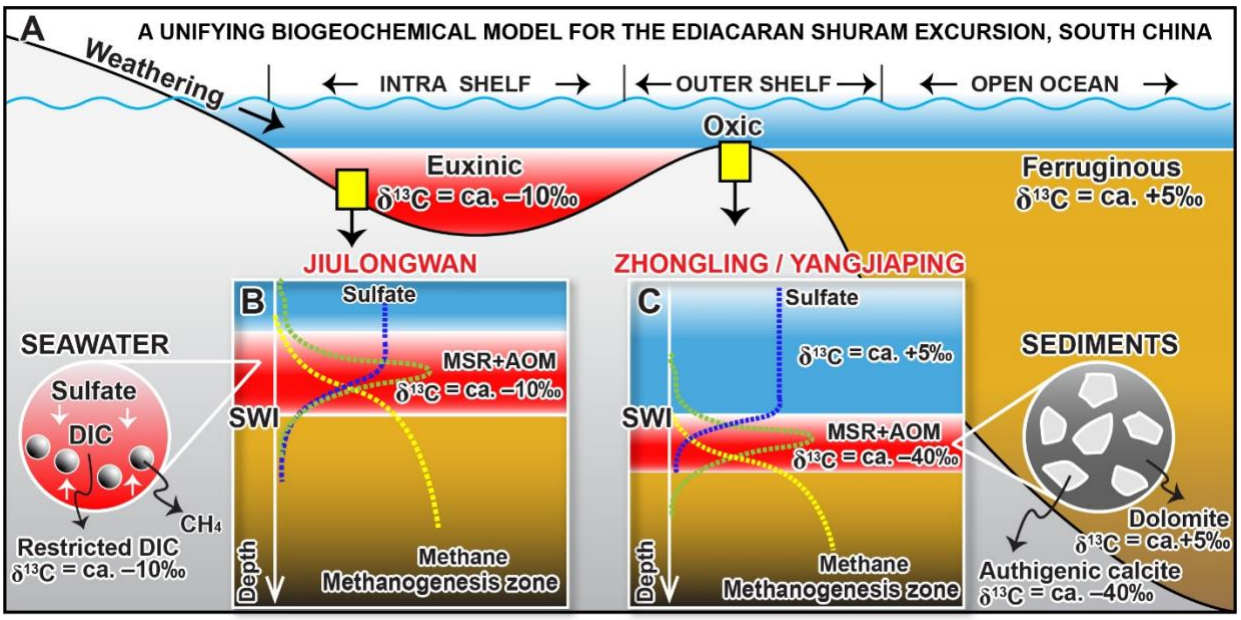

807

808 **Figure 17.** Conceptual biogeochemical model for the Shuram excursion based on investigations of the
809 upper Doushantuo Formation at intra shelf (Jiulongwan) and outer shelf (Zhongling and Yangjiaping)
810 sections, South China. (**A**) Reconstructed redox conditions based on previous studies (Li et al., 2010; Jiang
811 et al., 2011; Cui et al., 2015). (**B**) The Jiulongwan section is characterized by anoxic/euxinic lagoonal
812 environment with MSR and AOM occurring in water column. Zoomed-in circle on the left-hand side shows
813 marine DIC mixed with methane-derived alkalinity in the restricted euxinic water column. **(C)** The
814 Zhongling and Yangjiaping sections are characterized by more oxygenated marine shelf environment with
815 sulfate-methane transition zone (SMTZ) located in shallow marine sediments. Zoomed-in circle on the
816 right-hand side shows dolomicrite matrix and methane-derived authigenic calcite cements within shallow
817 marine sediments. See detailed discussion in main text. Abbreviations: MSR = microbial sulfate reduction;
818 AOM = anaerobic oxidation of methane; SWI = sediment-water interface; DIC = dissolved inorganic
819 carbon.

820

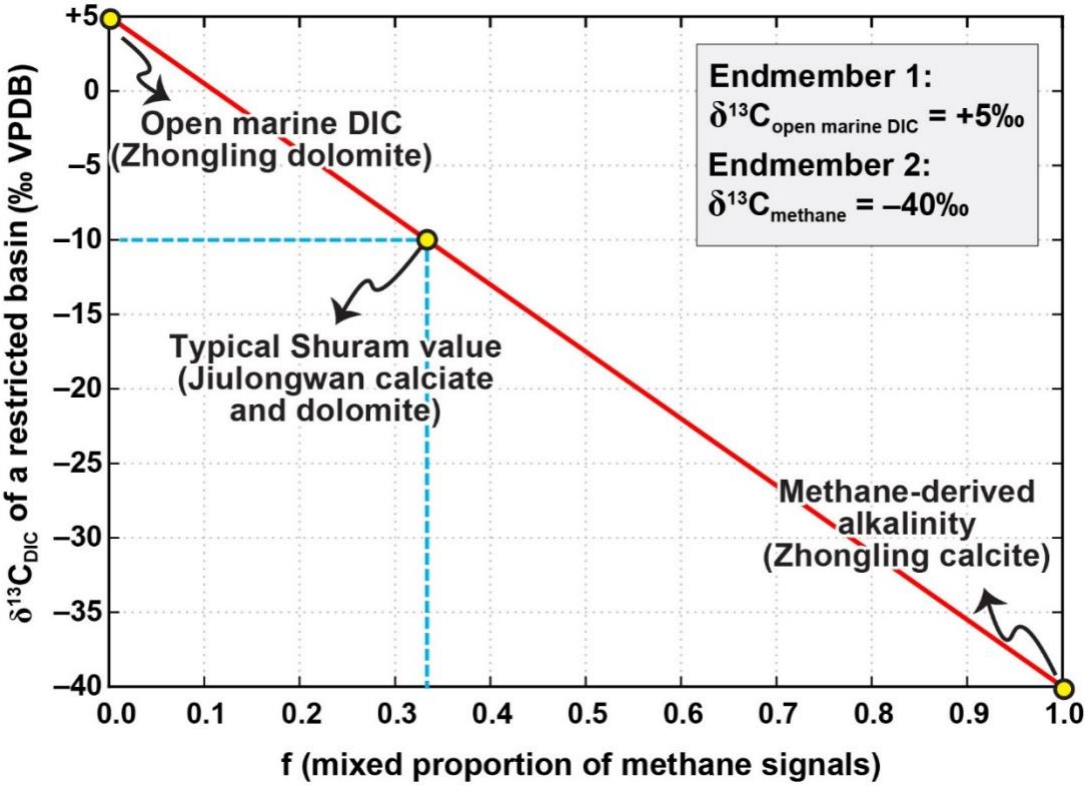

Fig. 18. A simple two-endmember mixing model, with open marine dissolved inorganic carbon ($\delta^{13}C_{open\ marine\ DIC}$ = +5‰) as endmember 1 and methane flux ($\delta^{13}C_{methane}$ = –40‰) as endmember 2. The isotopic values of these two endmembers are based on SIMS results in this study. The X-axis represents mixing proportion of methane. The Y-axis represents the carbon isotope values of the mixture (e.g., DIC in a restricted basin). Abbreviation: DIC = dissolved inorganic carbon.

REFERENCES

Ader, M., Macouin, M., Trindade, R.I.F., Hadrien, M.-H., Yang, Z., Sun, Z., Besse, J., 2009. A multilayered water column in the Ediacaran Yangtze platform? Insights from carbonate and organic matter paired $\delta^{13}C$. Earth and Planetary Science Letters, 288, 213–227. https://dx.doi.org/10.1016/j.epsl.2009.09.024.

An, Z., Jiang, G., Tong, J., Tian, L., Ye, Q., Song, H., Song, H., 2015. Stratigraphic position of the Ediacaran Miaohe biota and its constrains on the age of the upper Doushantuo $\delta^{13}C$ anomaly in the Yangtze Gorges area, South China. Precambrian Research, 271, 243–253. https://dx.doi.org/10.1016/j.precamres.2015.10.007.

Andrieu, S., Brigaud, B., Barbarand, J., Lasseur, E., 2017. The complex diagenetic history of discontinuities in shallow-marine carbonate rocks: New insights from high-resolution ion microprobe investigation of $\delta^{18}O$ and $\delta^{13}C$ of early cements. Sedimentology, 65, 360–399. https://dx.doi.org/10.1111/sed.12384.

Burns, S.J., Matter, A., 1993. Carbon isotopic record of the latest Proterozoic from Oman. Eclogae Geologicae Helvetiae, 86, 595–607. https://dx.doi.org/10.5169/seals-167254.

Burns, S.J., Haudenschild, U., Matter, A., 1994. The strontium isotopic composition of carbonates from the late Precambrian (~560–540 Ma) Huqf Group of Oman. Chemical Geology, 111, 269–282. https://dx.doi.org/10.1016/0009-2541(94)90094-9.

Calver, C.R., 2000. Isotope stratigraphy of the Ediacarian (Neoproterozoic III) of the Adelaide Rift Complex, Australia, and the overprint of water column stratification. Precambrian Research, 100, 121–150. https://dx.doi.org/10.1016/s0301-9268(99)00072-8.

Chang, B., Li, C., Liu, D., Foster, I., Tripati, A., Lloyd, M.K., Maradiaga, I., Luo, G., An, Z., She, Z., Xie, S., Tong, J., Huang, J., Algeo, T.J., Lyons, T.W., Immenhauser, A., 2020. Massive formation of early diagenetic dolomite in the Ediacaran ocean: Constraints on the "dolomite problem". Proceedings of the National Academy of Sciences, 117, 14005–14014. https://dx.doi.org/10.1073/pnas.1916673117.

Chen, Z., Zhou, C., Meyer, M., Xiang, K., Schiffbauer, J.D., Yuan, X., Xiao, S., 2013. Trace fossil evidence for Ediacaran bilaterian animals with complex behaviors. Precambrian Research, 224, 690–701. https://dx.doi.org/10.1016/j.precamres.2012.11.004.

Condon, D., Zhu, M., Bowring, S., Wang, W., Yang, A., Jin, Y., 2005. U–Pb ages from the Neoproterozoic Doushantuo Formation, China. Science, 308, 95–98. https://dx.doi.org/10.1126/science.1107765.

Cui, H., Kaufman, A.J., Xiao, S., Zhu, M., Zhou, C., Liu, X.-M., 2015. Redox architecture of an Ediacaran ocean margin: Integrated chemostratigraphic ($\delta^{13}C$–$\delta^{34}S$–$^{87}Sr/^{86}Sr$–Ce/Ce*) correlation of the Doushantuo Formation, South China. Chemical Geology, 405, 48–62. https://dx.doi.org/10.1016/j.chemgeo.2015.04.009.

Cui, H., Xiao, S., Zhou, C., Peng, Y., Kaufman, A.J., Plummer, R.E., 2016. Phosphogenesis associated with the Shuram Excursion: Petrographic and geochemical observations from the Ediacaran Doushantuo Formation of South China. Sedimentary Geology, 341, 134–146. https://dx.doi.org/10.1016/j.sedgeo.2016.05.008.

Cui, H., Kaufman, A.J., Xiao, S., Zhou, C., Liu, X.-M., 2017. Was the Ediacaran Shuram Excursion a globally synchronized early diagenetic event? Insights from methane-derived authigenic carbonates in the uppermost Doushantuo Formation, South China. Chemical Geology, 450, 59–80. https://dx.doi.org/10.1016/j.chemgeo.2016.12.010.

Cui, H., Orland, I.J., Denny, A., Kitajima, K., Fournelle, J.H., Baele, J.-M., de Winter, N.J., Goderis, S., Claeys, P., Valley, J.W., 2019. Ice or fire? Constraining the origin of

isotopically anomalous cap carbonate cements by SIMS, Geological Society of America Abstracts with Programs. Vol. 51, No. 5, Phoenix, Arizona, USA https://dx.doi.org/10.1130/abs/2019AM-332456.

Cui, H., Kaufman, A.J., Zou, H., Kattan, F.H., Trusler, P., Smith, J., Yu. Ivantsov, A., Rich, T.H., Al Qubsani, A., Yazedi, A., Liu, X.-M., Johnson, P., Goderis, S., Claeys, P., Vickers-Rich, P., 2020. Primary or secondary? A dichotomy of the strontium isotope anomalies in the Ediacaran carbonates of Saudi Arabia. Precambrian Research, 343, 105720. https://dx.doi.org/10.1016/j.precamres.2020.105720.

Cui, H., Kitajima, K., Orland, I.J., Xiao, S., Kaufman, A.J., Denny, A., Baele, J.-M., Zhou, C., Spicuzza, M.J., Fournelle, J.H., Valley, J.W., 2021. Deposition or diagenesis? Probing the Ediacaran Shuram excursion in South China by SIMS. Global and Planetary Change, Under review.

Denny, A.C., Kozdon, R., Kitajima, K., Valley, J.W., 2017. Isotopically zoned carbonate cements in Early Paleozoic sandstones of the Illinois Basin: $\delta^{18}O$ and $\delta^{13}C$ records of burial and fluid flow. Sedimentary Geology, 361, 93–110. https://dx.doi.org/10.1016/j.sedgeo.2017.09.004.

Denny, A.C., Orland, I.J., Valley, J.W., 2020. Regionally correlated oxygen and carbon isotope zonation in diagenetic carbonates of the Bakken Formation. Chemical Geology, 531, 119327. https://dx.doi.org/10.1016/j.chemgeo.2019.119327.

Donovan, J.J., Tingle, T.N., 1996. An improved mean atomic number background correction for quantitative microanalysis. Microscopy and Microanalysis, 2, 1–7.

Donovan, J.J., Kremser, D., Fournelle, J., Goemann, K., 2018. Probe for Windows User's Guide and Reference, Enterprise Edition. Probe Software, Inc., Eugene, OR

Fike, D.A., Grotzinger, J.P., Pratt, L.M., Summons, R.E., 2006. Oxidation of the Ediacaran ocean. Nature, 444, 744–747. https://dx.doi.org/10.1038/nature05345.

Furuyama, S., Kano, A., Kunimitsu, Y., Ishikawa, T., Wei, W., 2016. Diagenetic overprint to a negative carbon isotope anomaly associated with the Gaskiers glaciation of the Ediacaran Doushantuo Formation in South China. Precambrian Research, 110–122. https://dx.doi.org/10.1016/j.precamres.2016.01.004.

Gillhaus, A., Richter, D.K., Götte, T., Neuser, R.D., 2010. From tabular to rhombohedral dolomite crystals in Zechstein 2 dolostones from Scharzfeld (SW Harz/Germany): A case study with combined CL and EBSD investigations. Sedimentary geology, 228, 284–291. https://dx.doi.org/10.1016/j.sedgeo.2010.05.003.

Grotzinger, J.P., Fike, D.A., Fischer, W.W., 2011. Enigmatic origin of the largest-known carbon isotope excursion in Earth's history. Nature Geoscience, 4, 285–292. https://dx.doi.org/10.1038/ngeo1138.

Halverson, G.P., Hoffman, P.F., Schrag, D.P., Maloof, A.C., Rice, A.H.N., 2005. Toward a Neoproterozoic composite carbon-isotope record. Geological Society of America Bulletin, 117, 1181–1207. https://dx.doi.org/10.1130/b25630.1.

Hood, A.v.S., Wallace, M.W., 2012. Synsedimentary diagenesis in a Cryogenian reef complex: Ubiquitous marine dolomite precipitation. Sedimentary Geology, 255–256, 56–71. https://dx.doi.org/10.1016/j.sedgeo.2012.02.004.

Hood, A.v.S., Wallace, M.W., Reed, C.P., Hoffmann, K.H., Freyer, E.E., 2015. Enigmatic carbonates of the Ombombo Subgroup, Otavi Fold Belt, Namibia: A prelude to extreme Cryogenian anoxia? Sedimentary Geology, 324, 12–31. https://dx.doi.org/10.1016/j.sedgeo.2015.04.007.

Hood, A.v.S., Wallace, M.W., 2018. Neoproterozoic marine carbonates and their paleoceanographic significance. Global and Planetary Change, 160, 28–45. https://dx.doi.org/10.1016/j.gloplacha.2017.11.006.

Husson, J.M., Linzmeier, B.J., Kitajima, K., Ishida, A., Maloof, A.C., Schoene, B., Peters, S.E., Valley, J.W., 2020. Large isotopic variability at the micron-scale in 'Shuram' excursion carbonates from South Australia. Earth and Planetary Science Letters, 538, 116211. https://dx.doi.org/10.1016/j.epsl.2020.116211.

Jiang, G., Kaufman, A.J., Christie-Blick, N., Zhang, S., Wu, H., 2007. Carbon isotope variability across the Ediacaran Yangtze platform in South China: Implications for a large surface-to-deep ocean $\delta^{13}C$ gradient. Earth and Planetary Science Letters, 261, 303–320. https://dx.doi.org/10.1016/j.epsl.2007.07.009.

Jiang, G., Shi, X., Zhang, S., Wang, Y., Xiao, S., 2011. Stratigraphy and paleogeography of the Ediacaran Doushantuo Formation (ca. 635–551Ma) in South China. Gondwana Research, 19, 831–849. https://dx.doi.org/10.1016/j.gr.2011.01.006.

Kaufman, A.J., Knoll, A.H., 1995. Neoproterozoic variations in the C-isotopic composition of seawater: stratigraphic and biogeochemical implications. Precambrian Research, 73, 27–49. https://dx.doi.org/10.1016/0301-9268(94)00070-8.

Kaufman, A.J., Knoll, A.H., Narbonne, G.M., 1997. Isotopes, ice ages, and terminal Proterozoic earth history. Proceedings of the National Academy of Sciences, 94, 6600–6605.

Kozdon, R., Ushikubo, T., Kita, N.T., Spicuzza, M., Valley, J.W., 2009. Intratest oxygen isotope variability in the planktonic foraminifer *N. pachyderma*: Real vs. apparent vital effects by ion microprobe. Chemical Geology, 258, 327–337. https://dx.doi.org/10.1016/j.chemgeo.2008.10.032.

Kunimitsu, Y., Setsuda, Y., Furuyama, S., Wang, W., Kano, A., 2011. Ediacaran chemostratigraphy and paleoceanography at a shallow marine setting in northwestern Hunan Province, South China. Precambrian Research, 191, 194–208. https://dx.doi.org/10.1016/j.precamres.2011.09.006.

Le Guerroué, E., Allen, P.A., Cozzi, A., Etienne, J.L., Fanning, M., 2006. 50 Myr recovery from the largest negative $\delta^{13}C$ excursion in the Ediacaran ocean. Terra Nova, 18, 147–153. https://dx.doi.org/10.1111/j.1365-3121.2006.00674.x.

Li, C., Love, G.D., Lyons, T.W., Fike, D.A., Sessions, A.L., Chu, X., 2010. A stratified redox model for the Ediacaran ocean. Science, 328, 80–83. https://dx.doi.org/10.1126/science.1182369.

Li, C., Hardisty, D.S., Luo, G., Huang, J., Algeo, T.J., Cheng, M., Shi, W., An, Z., Tong, J., Xie, S., Jiao, N., Lyons, T.W., 2017. Uncovering the spatial heterogeneity of Ediacaran carbon cycling. Geobiology, 15, 211–224. https://dx.doi.org/10.1111/gbi.12222.

Li, Z., Cao, M., Loyd, S.J., Algeo, T.J., Zhao, H., Wang, X., Zhao, L., Chen, Z.-Q., 2020. Transient and stepwise ocean oxygenation during the late Ediacaran Shuram Excursion: Insights from carbonate $\delta^{238}U$ of northwestern Mexico. Precambrian Research, 344, 105741. https://dx.doi.org/10.1016/j.precamres.2020.105741.

Ling, H.-F., Chen, X., Li, D., Wang, D., Shields-Zhou, G.A., Zhu, M., 2013. Cerium anomaly variations in Ediacaran–earliest Cambrian carbonates from the Yangtze Gorges area, South China: Implications for oxygenation of coeval shallow seawater. Precambrian Research, 225, 110–127. https://dx.doi.org/10.1016/j.precamres.2011.10.011.

Lu, M., Zhu, M., Zhang, J., Shields-Zhou, G., Li, G., Zhao, F., Zhao, X., Zhao, M., 2013. The DOUNCE event at the top of the Ediacaran Doushantuo Formation, South China: Broad

stratigraphic occurrence and non-diagenetic origin. Precambrian Research, 225, 86–109. https://dx.doi.org/10.1016/j.precamres.2011.10.018.

Macouin, M., Besse, J., Ader, M., Gilder, S., Yang, Z., Sun, Z., Agrinier, P., 2004. Combined paleomagnetic and isotopic data from the Doushantuo carbonates, South China: implications for the "snowball Earth" hypothesis. Earth and Planetary Science Letters, 224, 387–398. https://dx.doi.org/10.1016/j.epsl.2004.05.015.

Macouin, M., Ader, M., Moreau, M.-G., Poitou, C., Yang, Z., Sun, Z., 2012. Deciphering the impact of diagenesis overprint on negative $\delta^{13}C$ excursions using rock magnetism: Case study of Ediacaran carbonates, Yangjiaping section, South China. Earth and Planetary Science Letters, 351–352, 281–294. https://dx.doi.org/10.1016/j.epsl.2012.06.057.

McFadden, K.A., Huang, J., Chu, X., Jiang, G., Kaufman, A.J., Zhou, C., Yuan, X., Xiao, S., 2008. Pulsed oxidation and biological evolution in the Ediacaran Doushantuo Formation. Proceedings of the National Academy of Sciences, 105, 3197–3202. https://dx.doi.org/10.1073/pnas.0708336105.

Melezhik, V.A., Pokrovsky, B.G., Fallick, A.E., Kuznetsov, A.B., Bujakaite, M.I., 2009. Constraints on $^{87}Sr/^{86}Sr$ of Late Ediacaran seawater: insight from Siberian high-Sr limestones. Journal of the Geological Society, 166, 183–191. https://dx.doi.org/10.1144/0016-76492007-171.

Narbonne, G.M., Xiao, S., Shields, G.A., Gehling, J.G., 2012. The Ediacaran Period. In: Gradstein, F.M., Ogg, J.G., Schmitz, M.D., Ogg, G.M. (Eds.), The Geologic Time Scale. Elsevier, Boston, USA, pp. 413–435. https://dx.doi.org/10.1016/b978-0-444-59425-9.00018-4.

Sawaki, Y., Ohno, T., Tahata, M., Komiya, T., Hirata, T., Maruyama, S., Windley, B.F., Han, J., Shu, D., Li, Y., 2010. The Ediacaran radiogenic Sr isotope excursion in the Doushantuo Formation in the Three Gorges area, South China. Precambrian Research, 176, 46–64. https://dx.doi.org/10.1016/j.precamres.2009.10.006.

Schmitz, M.D., 2012. Radiometric ages used in GTS2012. In: Gradstein, F.M., Ogg, J.G., Schmitz, M.D., Ogg, G.M. (Eds.), The Geologic Time Scale. Elsevier, Boston, pp. 1045–1082. https://dx.doi.org/10.1016/b978-0-444-59425-9.15002-4.

Schrag, D.P., Higgins, J.A., Macdonald, F.A., Johnston, D.T., 2013. Authigenic carbonate and the history of the global carbon cycle. Science, 339, 540–543. https://dx.doi.org/10.1126/science.1229578.

Shi, W., Li, C., Luo, G., Huang, J., Algeo, T.J., Jin, C., Zhang, Z., Cheng, M., 2018. Sulfur isotope evidence for transient marine-shelf oxidation during the Ediacaran Shuram Excursion. Geology, 46, 267–270. https://dx.doi.org/10.1130/g39663.1.

Śliwiński, M.G., Kitajima, K., Kozdon, R., Spicuzza, M.J., Fournelle, J.H., Denny, A., Valley, J.W., 2016a. Secondary ion mass spectrometry bias on isotope ratios in dolomite–ankerite, Part II: $\delta^{13}C$ matrix effects. Geostandards and Geoanalytical Research, 40, 173–184. https://dx.doi.org/10.1111/j.1751-908X.2015.00380.x.

Śliwiński, M.G., Kozdon, R., Kitajima, K., Valley, J.W., Denny, A., 2016b. Microanalysis of carbonate cement $\delta^{18}O$ in a CO_2-storage system seal: insights into the diagenetic history of the Eau Claire Formation (Upper Cambrian), Illinois Basin. AAPG Bulletin, 1003–1031. https://dx.doi.org/10.1306/02031615065.

Śliwiński, M.G., Kitajima, K., Kozdon, R., Spicuzza, M.J., Denny, A., Valley, J.W., 2017. In situ $\delta^{13}C$ and $\delta^{18}O$ microanalysis by SIMS: A method for characterizing the carbonate

components of natural and engineered CO2-reservoirs. International Journal of Greenhouse Gas Control, 57, 116–133. https://dx.doi.org/10.1016/j.ijggc.2016.12.013.
Tahata, M., Ueno, Y., Ishikawa, T., Sawaki, Y., Murakami, K., Han, J., Shu, D., Li, Y., Guo, J., Yoshida, N., Komiya, T., 2013. Carbon and oxygen isotope chemostratigraphies of the Yangtze platform, South China: Decoding temperature and environmental changes through the Ediacaran. Gondwana Research, 23, 333–353. https://dx.doi.org/10.1016/j.gr.2012.04.005.
Tucker, M.E., 1982. Precambrian dolomites: petrographic and isotopic evidence that they differ from Phanerozoic dolomites. Geology, 10, 7–12. https://dx.doi.org/10.1130/0091-7613(1982)10<7:PDPAIE>2.0.CO;2.
Valley, J.W., Kita, N.T., 2009. *In situ* oxygen isotope geochemistry by ion microprobe. In: Fayek, M. (Ed.), Secondary Ion Mass Spectrometry in the Earth Sciences – Gleaning the Big Picture from a Small Spot. Mineralogical Association of Canada Short Course 41, Toronto, pp. 19–63.
Wallmann, K., Aloisi, G., 2012. The Global Carbon Cycle: Geological Processes. In: Knoll, A.H., Canfield, D.E., Konhauser, K.O. (Eds.), Fundamentals of Geobiology. Blackwell Publishing Ltd, Hoboken, New Jersey, USA, pp. 20–35. https://dx.doi.org/10.1002/9781118280874.ch3.
Wang, W., Zhou, C., Yuan, X., Chen, Z., Xiao, S., 2012. A pronounced negative $\delta^{13}C$ excursion in an Ediacaran succession of western Yangtze Platform: A possible equivalent to the Shuram event and its implication for chemostratigraphic correlation in South China. Gondwana Research, 22, 1091–1101. https://dx.doi.org/10.1016/j.gr.2012.02.017.
Wang, W., Guan, C., Hu, Y., Cui, H., Muscente, A.D., Chen, L., Zhou, C., 2020. Spatial and temporal evolution of Ediacaran carbon and sulfur cycles in the Lower Yangtze Block, South China. Palaeogeography, Palaeoclimatology, Palaeoecology, 537, 109417. https://dx.doi.org/10.1016/j.palaeo.2019.109417.
Wang, X., Jiang, G., Shi, X., Xiao, S., 2016. Paired carbonate and organic carbon isotope variations of the Ediacaran Doushantuo Formation from an upper slope section at Siduping, South China. Precambrian Research, 273, 53–66. https://dx.doi.org/10.1016/j.precamres.2015.12.010.
Wei, W., Frei, R., Gilleaudeau, G.J., Li, D., Wei, G.-Y., Chen, X., Ling, H.-F., 2018. Oxygenation variations in the atmosphere and shallow seawaters of the Yangtze Platform during the Ediacaran Period: Clues from Cr-isotope and Ce-anomaly in carbonates. Precambrian Research, 313, 78–90. https://dx.doi.org/10.1016/j.precamres.2018.05.009.
Wycech, J.B., Kelly, D.C., Kozdon, R., Orland, I.J., Spero, H.J., Valley, J.W., 2018. Comparison of $\delta^{18}O$ analyses on individual planktic foraminifer (*Orbulina universa*) shells by SIMS and gas-source mass spectrometry. Chemical Geology, 483, 119–130. https://dx.doi.org/10.1016/j.chemgeo.2018.02.028.
Xiao, S., Narbonne, G.M., Zhou, C., Laflamme, M., Grazhdankin, D.V., Moczydłowska-Vidal, M., Cui, H., 2016. Toward an Ediacaran time scale: Problems, protocols, and prospects. Episodes, 39, 540–555. https://dx.doi.org/10.18814/epiiugs/2016/v39i4/103886.
Xiao, S., Cui, H., Kang, J., Mcfadden, K.A., Kaufman, A.J., Kitajima, K., Fournelle, J.H., Valley, J.W., 2019. Using SIMS data to understand the role of authigenic carbonate in the origin of chaotic stratigraphic variations of carbon isotopes in the early Ediacaran Doushantuo Formation, Geological Society of America annual meeting, Phoenix, Arizona, USA https://dx.doi.org/10.1130/abs/2019AM-335046.

Xiao, S., Cui, H., Kang, J., McFadden, K.A., Kaufman, A.J., Kitajima, K., Fournelle, J.H., Schwid, M., Nolan, M., Baele, J.-M., Valley, J.W., 2020. Using SIMS to decode noisy stratigraphic $\delta^{13}C$ variations in Ediacaran carbonates. Precambrian Research, 343, 105686. https://dx.doi.org/10.1016/j.precamres.2020.105686.

Zhang, F., Xiao, S., Romaniello, S.J., Hardisty, D., Li, C., Melezhik, V., Pokrovsky, B., Cheng, M., Shi, W., Lenton, T.M., Anbar, A.D., 2019. Global marine redox changes drove the rise and fall of the Ediacara biota. Geobiology, 17, 594–610. https://dx.doi.org/10.1111/gbi.12359.

Zhou, C., Xiao, S., 2007. Ediacaran $\delta^{13}C$ chemostratigraphy of South China. Chemical Geology, 237, 89–108. https://dx.doi.org/10.1016/j.chemgeo.2006.06.021.

Zhou, C., Jiang, S., Xiao, S., Chen, Z., Yuan, X., 2012. Rare earth elements and carbon isotope geochemistry of the Doushantuo Formation in South China: Implication for middle Ediacaran shallow marine redox conditions. Chinese Science Bulletin, 57, 1998–2006. https://dx.doi.org/10.1007/s11434-012-5082-6.

Zhou, C., Xiao, S., Wang, W., Guan, C., Ouyang, Q., Chen, Z., 2017. The stratigraphic complexity of the middle Ediacaran carbon isotopic record in the Yangtze Gorges area, South China, and its implications for the age and chemostratigraphic significance of the Shuram excursion. Precambrian Research, 288, 23–38. https://dx.doi.org/10.1016/j.precamres.2016.11.007.

Zhu, M., Strauss, H., Shields, G.A., 2007a. From snowball earth to the Cambrian bioradiation: calibration of Ediacaran–Cambrian earth history in South China. Palaeogeography, Palaeoclimatology, Palaeoecology, 254, 1–6. https://dx.doi.org/10.1016/j.palaeo.2007.03.026.

Zhu, M., Zhang, J., Yang, A., 2007b. Integrated Ediacaran (Sinian) chronostratigraphy of South China. Palaeogeography, Palaeoclimatology, Palaeoecology, 254, 7–61. https://dx.doi.org/10.1016/j.palaeo.2007.03.025.

Zhu, M., Lu, M., Zhang, J., Zhao, F., Li, G., Yang, A., Zhao, X., Zhao, M., 2013. Carbon isotope chemostratigraphy and sedimentary facies evolution of the Ediacaran Doushantuo Formation in western Hubei, South China. Precambrian Research, 225, 7–28. https://dx.doi.org/10.1016/j.precamres.2011.07.019.